AGU ADVANCING EARTH AND SPACE SCIENCES

Water Resources Research®

RESEARCH ARTICLE
10.1029/2025WR041424

Semi-Analytical Models for Predicting the Maximum Longitudinal Flow Velocity in the Confluence Channel

Haokun Feng[1], Zhiwei Li[1,2], Carlo Gualtieri[3], Bin Sun[1,2], Feifei Wang[1,2], and Kun Li[4]

[1]School of Water Conservancy and Transportation, Zhengzhou University, Zhengzhou, China, [2]Yellow River Laboratory, Zhengzhou University, Zhengzhou, China, [3]Department of Structures for Engineering and Architecture, University of Napoli Federico II, Napoli, Italy, [4]Yellow River Engineering Consulting Co. Ltd, Zhengzhou, China

Key Points:

- The reasons for the formation of the maximum flow velocity are investigated by laboratory experiments and numerical simulations
- The maximum velocity at the cross-section with the widest recirculation zone can be used as a proxy for the peak velocity calculation
- Semi-analytical models for maximum longitudinal velocity were derived using the control volume method and double-layer assumption

Supporting Information:

Supporting Information may be found in the online version of this article.

Correspondence to:

Z. Li,
zwli@zzu.edu.cn

Citation:

Feng, H., Li, Z., Gualtieri, C., Sun, B., Wang, F., & Li, K. (2025). Semi-analytical models for predicting the maximum longitudinal flow velocity in the confluence channel. *Water Resources Research*, *61*, e2025WR041424. https://doi.org/10.1029/2025WR041424

Received 22 JUN 2025
Accepted 11 NOV 2025

Author Contributions:

Conceptualization: Zhiwei Li
Data curation: Haokun Feng
Formal analysis: Haokun Feng
Funding acquisition: Zhiwei Li, Bin Sun
Investigation: Haokun Feng, Feifei Wang, Kun Li
Methodology: Haokun Feng, Zhiwei Li
Project administration: Zhiwei Li
Resources: Haokun Feng, Feifei Wang
Software: Zhiwei Li
Supervision: Zhiwei Li
Validation: Haokun Feng
Visualization: Haokun Feng
Writing – original draft: Haokun Feng
Writing – review & editing: Zhiwei Li, Carlo Gualtieri

Abstract In a channel confluence, different hydrodynamic characteristics can significantly affect the flow structure. As the main and tributary flow converges at the confluence, they are constrained by the recirculation zone, resulting in streamline contraction and an increase in flow velocity, thereby creating a zone of maximum velocity adjacent to the maximum width of the recirculation zone. The maximum flow velocity governs pollutant transport about a confluence and also influences bed erosion; thus, an accurate determination of the maximum flow velocity is crucial. In the present study, a statistical methodology was applied to validate the feasibility of substituting the maximum flow velocity at the widest section of the recirculation zone with the longitudinal maximum flow velocity. Two distinct models were formulated to address the transition between two mixing modes in the shear layer. In the wake mode, the two-control volume approach was applied, using the lowest velocity within the shear layer as a boundary to partition the contracted flow into two control volumes. In the mixing-layer mode, the contracted flow was treated as a single control volume. Those semi-analytical models were validated using 3D numerical results and experimental data collected in laboratory-scale confluence. The validation results demonstrate that both the proposed models could be applied to their respective shear layer modes to accurately predict the maximum longitudinal flow velocity.

1. Introduction

Confluence channels constitute a critical component of riverine network structures and are prevalent in urban drainage as well as agricultural irrigation systems. Confluence channels are often accompanied by intricate hydrodynamic features (Gualtieri et al., 2020; Lewis et al., 2020; Ramamurthy et al., 1994; Ribeiro et al., 2012; Yuan, Xu, et al., 2022, 2023), which influence bedform morphology (Best, 1988; Canelas et al., 2022; Cheng & Constantinescu, 2018), sediment transport (Gualtieri et al., 2019; Umar et al., 2018), pollutant dispersal (Cuss et al., 2021; Zhang et al., 2023), and thermal mixing processes (Rhoads & Johnson, 2018). Best (1987) delineated six types of flow features in confluence channels: the flow stagnation zone, flow deflection zone, flow separation zone, maximum velocity zone, flow recovery zone, and shear layers. These hydrodynamic characteristics markedly affect the velocity distribution within the confluence channel.

Secondary flows, akin to those observed in curved channels, are frequently observed within the confluence hydrodynamics zone (CHZ), defined as the zone within, upstream and downstream of the confluence affected by flow convergence (Kenworthy & Rhoads, 1995). The secondary flows are attributed to the imbalance between centrifugal force and pressure gradient force (Li et al., 2022; Lyubimova et al., 2020). Secondary flow not only modifies the velocity and shear stress distribution at the confluence but also amplifies the exchange and transport of energy and mass in the flow field (Kim et al., 2020; Vinuesa et al., 2018; Xu et al., 2022). The flow velocities in the confluence rivers are influenced not only by secondary flows but also by the compression effect of the separation zone (Schindfessel et al., 2015). Best (1987) discovered a shear layer forming between the two converging flows, and Constantinescu, Miyawaki, et al. (2011) noted that the quasi-two-dimensional vortex structures in the shear layer resemble that of a wake behind a bluff body, with continuous vortices rotating in opposite directions. Numerical modeling serves as a pivotal tool for investigating hydrodynamics in confluent channels (Constantinescu & Gualtieri, 2024). Such models have been employed to explore flow characteristics in these regions, with one-dimensional (Rice et al., 2006), two-dimensional (Constantinescu, Koken, & Zeng, 2011; Ghostine et al., 2010; Lewis & Rhoads, 2015), and three-dimensional models (Bradbrook et al., 1998, 2000; Chen et al., 2017; Luo et al., 2018) progressively developed.

It is of paramount importance to determine the position and magnitude of the maximum flow velocity. The formation of scour holes in the confluence channel is associated with the depression of the core of maximum velocity and/or intense shear toward the bed by downwelling flow or secondary flows (Ashmore, 1982; Ashmore et al., 1992; Yuan et al., 2018). Despite the lack of a unified conclusion regarding the causes of scour hole formation, maximum flow velocity remains one of the key factors contributing to their development. Flow velocity plays a critical role in governing pollutant adsorption at the sediment-water interface (Smith, 2009; Yang & Cheng, 2016). Higher velocities reduce the retention capacity of bed sediments and shorten water-sediment contact time, resulting in a distinct low-adsorption zone near the region of maximum velocity (Liu et al., 2019; Xiao et al., 2017, 2019). This phenomenon enhances downstream pollutant transport (Shi et al., 2025) and improves mixing efficiency (Zhang et al., 2023). Soluble pollutants such as PO_4^{3-} readily combine with organic matter (Wang et al., 2006) and cations (e.g., Cu^{2+}, Zn^{2+}, Fe^{3+}, Al^{3+}) that are adsorbed on sediment surfaces (Danen-Louwerse et al., 1993; Lopez et al., 1996; Yuan et al., 2019; Zhou et al., 2005), forming colloidal suspensions (Schemel et al., 2007; Xiao et al., 2015), which contribute to the formation of contaminated sediment. Turbulence within the shear layer inhibits flocculation of these contaminated sediments (Yuan et al., 2019), while the maximum velocity near this zone promotes their downstream transport by high-speed flows. For pollutants adsorbed onto the bed surface, elevated flow velocities facilitate their remobilization into the water column (Liu et al., 2021, 2024; Shi et al., 2025). Consequently, the maximum flow velocity significantly influences both the transport and adsorption of pollutants. A comprehensive understanding of the hydrodynamic conditions at the confluence is therefore vital for advancing our understanding of pollutant dispersion in watersheds (Liu et al., 2021; Yang et al., 2009; Yu et al., 2020).

Although the maximum longitudinal flow velocity at confluences can be obtained through numerical simulations and field observations, measuring the maximum flow velocity in open channels is a formidable endeavor. In extreme cases, direct measurement becomes infeasible or inadvisable (Kakavandi et al., 2024). The use of sophisticated numerical models to calculate longitudinal flow velocity requires the input of numerous empirical parameters and the completion of extensive computational efforts, rendering them less suitable for engineering design purposes.

In the maximum velocity zone, longitudinal velocity u is significantly larger than lateral velocity v and vertical velocity w. Therefore, the maximum flow velocity $\sqrt{u^2 + v^2 + w^2}$ is approximately equal to the maximum longitudinal velocity $u_{\max}$. Additionally, due to the presence of secondary flows, calculating v and w is highly challenging. Consequently, this study focuses on $u_{\max}$ as the primary research objective. The objective of this study is to develop a streamlined method for directly calculating $u_{\max}$. To address this issue, the control volume method, which divides the contraction zone into one or two control volumes based on the presence of the shear layer, is employed. Mathematical models were established using the two-layer hypothesis and mixing length theory within each control volume, and the accuracy of the model was validated through numerical simulations and flume experiments.

2. Experimental Setup and Instrumentation

A laboratory-scale confluence experiment was designed, incorporating two different junction angles θ (60° and 90°) and eight different discharge ratios η, based on values documented in natural confluence rivers (Boyer et al., 2006; Rhoads & Sukhodolov, 2008). Additionally, the experimental Froude numbers (0.29–0.41) fall within the range of values reported in previous field studies (0.03–0.85) and laboratory flume experiments (0.02–0.5; Yu et al., 2020). A total of 20 cases were listed in Table 1. The discharge ratio is expressed as $\eta = Q_t/(Q_t + Q_m)$, and the momentum ratio is expressed as $M_r = (Q_t u_t)/(Q_m u_m)$.

The laboratory-scale confluence had a main channel 14 m long and 1 m wide and a tributary channel 3 m long and 0.5 m wide (Figure 1). The bed and walls of the channel are made of glass, with a longitudinal slope of 0.01%. The water from the tank at the bottom of the channel is conveyed via a network of pipes to the upstream sections of the main and tributary channels. To achieve different discharge ratios, sewage pumps with powers of 15 and 5 kW are installed on the pipelines connecting the tank to the upstream sections of the main and tributary channels, respectively. The discharges in the main and tributary channels Q_m, and Q_t are gauged using ultrasonic flowmeters (accuracy: 0.1 m^3/hr) situated on the transport pipes. To ensure that the flow is fully developed before entering the confluence zone, honeycombs were installed upstream of the main and tributary channels. The water depth is

Table 1
Experiment Cases Under Different Discharge Ratios

60 90	A1 B1	A2 B2	A3 B3	A4 B4	A5 B5	A6 B6	A7 B7	A8 B8	A9 B9	A10 B10
Main-stream Discharge Q_m (m^3/s)	0.06	0.045	0.0321	0.0368	0.0329	0.0184	0.0184	0.0184	0.02305	0.0276
Main-stream velocity u_m (m/s)	0.423	0.3625	0.284	0.2895	0.2704	0.1861	0.1803	0.1695	0.2248	0.2509
Tributary Discharge Q_t (m^3/s)	0.00778	0.00778	0.0078	0.0139	0.0137	0.01	0.0125	0.015	0.00865	0.0104
Tributary velocity u_t (m/s)	0.1097	0.1253	0.138	0.2187	0.2253	0.2024	0.245	0.2764	0.1688	0.189
Froude	0.4053	0.3854	0.3354	0.3574	0.3508	0.2919	0.3028	0.2983	0.3085	0.3327
Reynolds number	60,170	60,170	60,170	60,170	60,170	60,170	60,170	60,170	60,170	60,170
W_d/H	7.75	9.22	10.78	9.47	9.64	13.94	13.70	13.1	12.79	11.32
Momentum ratio M_r	0.034	0.06	0.12	0.29	0.35	0.59	0.92	1.33	0.28	0.28
Discharge ratios η	0.11	0.15	0.20	0.27	0.29	0.35	0.40	0.45	0.27	0.27

Note. W_d represents the width of the main channel, and H represents the downstream water depth.

controlled by adjusting the opening of the tailgate located downstream. A schematic diagram of the experimental setup with a 90° junction angle is presented in Figure 2.

Identical instrumentation layouts and experimental apparatus were employed for 90° and 60° confluence configurations. Twenty-two measurement cross-sections were established. Initially 10 measurement cross-sections A-G were positioned with 10 cm intervals to monitor steep hydraulic gradients in both flow direction and depth profiles. This enhanced spatial resolution enables rigorous validation of the numerical framework while capturing the three-dimensional flow deflection characteristics of tributary inflow approaching the confluence apex. The subsequent 15 cross-sections H-V were positioned 20 cm apart, aimed at examining the maximum velocity zones and the boundaries of the recirculation area influenced by flow constriction. Twenty-one vertical lines were arranged across the measured cross-section, with a measurement point set at 3 cm intervals along the depth of each vertical line. The depth-measuring probe (accuracy: 0.1 mm) was positioned at the centroid of each velocity profile cross-section, corresponding to the transverse coordinate $y = 0.5$ m. Figure 3 illustrates the detailed arrangement of these measurement points across the cross-sections.

Figure 1. Global view of the 90° asymmetric confluence channel.

The three-dimensional velocities were measured using a SonTek 3D Acoustic Doppler Velocimeter (ADV, accuracy: 1 mm/s), which operates based on the Doppler effect, where ultrasonic waves emitted by the sensor probe are reflected by particles in the sample volume. The reflected signals are then received by the probe to determine the velocity of the particles, which is assumed to be equal to the flow velocity. The sampling volume is located 5 cm in front of the probe and has a volume of 0.42 cm^3. At each point, the measurement time and frequency were set to 60 s and 100 Hz. To ensure accurate flow velocity measurements, data with correlation coefficients greater than 85% and the signal-to-noise ratio (SNR) greater than 15 dB were retained. Talcum powder was added to the water throughout the entire experiment to enhance the acoustic signal. The ADV was fixed on a movable frame, and the position of the frame was manually adjusted and calibrated using a steel ruler (accuracy: 1 mm).

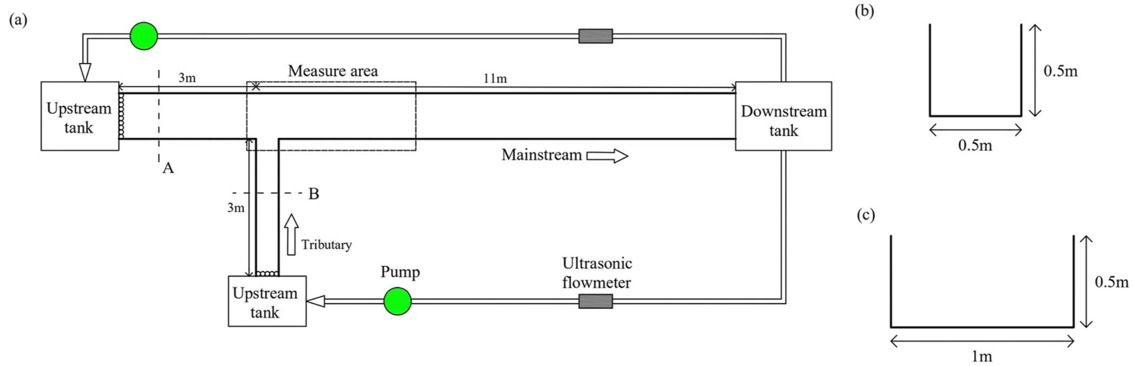

Figure 2. Sketch of the experimental setup: a confluence channel flume with a 90° junction angle. (a) Diagrammatic sketch in the horizontal plane; (b) Tribute upstream section B; (c) Mainstream upstream section A.

3. Numerical Model

The limited arrangement of measurement points prevented comprehensive coverage of the entire CHZ. Consequently, the maximum velocity could not be determined solely from experimental data. To resolve this, supplementary numerical simulations were conducted to obtain the maximum longitude velocity value.

3.1. Turbulence Model and Domain Meshes

The 3D model of the Reynolds-Averaged Navier-Stokes equations is solved in order to simulate the flow characteristics at the confluences. The continuity equation and momentum equations in the Cartesian coordinate system are as follows (Shen et al., 2023):

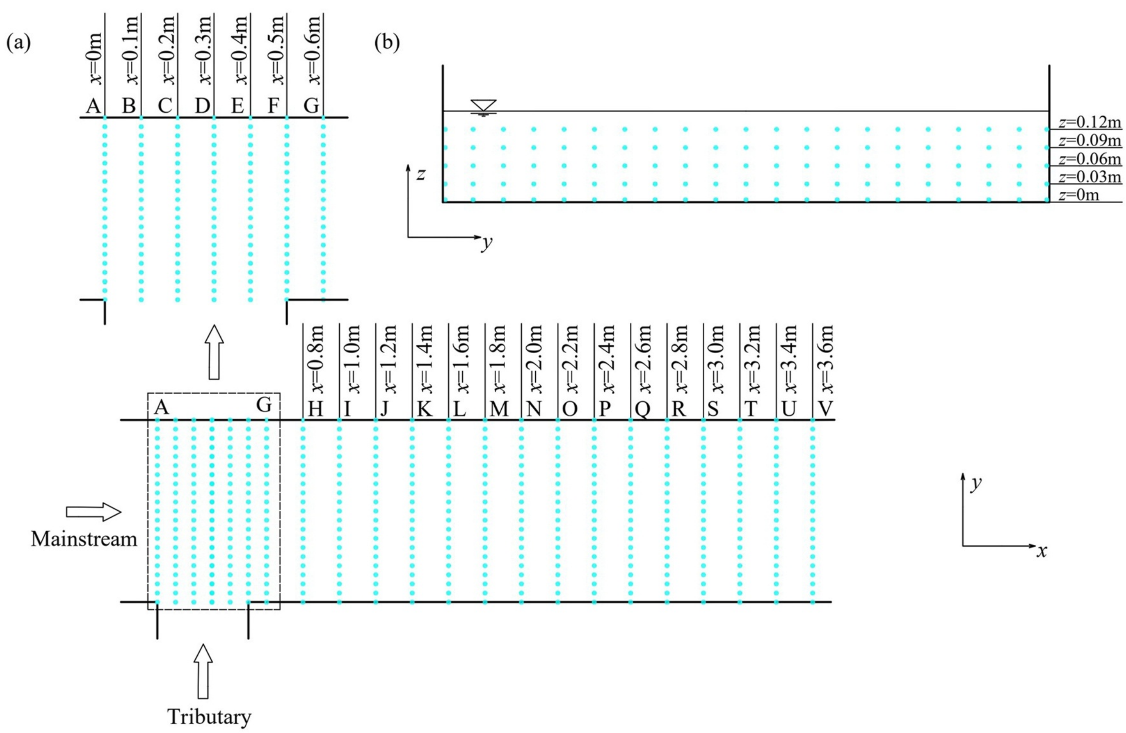

Figure 3. Schematic top view and cross-section of the measuring point arrangement, taking the 90° junction angle case, for example. (a) Horizontal measurement point; (b) Vertical measurement point.

$$\frac{\partial \rho}{\partial t} + \frac{\partial \rho u_i}{\partial x_i} = 0 \tag{1}$$

$$\frac{\partial \rho u_i}{\partial t} + \frac{\partial \rho u_j u_i}{\partial x_j} = -\frac{\partial p}{\partial x_i} + \frac{\partial}{\partial x_j}\left(\rho(\nu + \nu_t)\frac{\partial u_i}{\partial x_j}\right) \tag{2}$$

$$\nu_t = C_\mu \frac{k^2}{\varepsilon} \tag{3}$$

where t (s) is the time; u_i (m/s) is the flow velocity of each direction; ρ (kg/m^3) is the fluid density, with a constant of 998 kg/m^3; p (pa) is the pressure; ν (m^2/s) is the molecular kinematic viscosity coefficient; ν_t (m^2/s) is the eddy viscosity coefficient; g (m/s^2) is the acceleration of gravity; C_μ is an empirical constant, which was calculated as 0.085 (Shen et al., 2019); k (m^2/s^2) is the turbulent kinetic energy; ε (m^2/s^3) is the turbulent dissipation rate. The RNG k-ε model accurately performing to simulates flows with high strain rates and significant streamline curvature by adjusting turbulent viscosity and taking into account the effects of rotation and swirl flow. This results in more precise predictions of flow velocity and the dimensions of the recirculation zone in comparison to other turbulence models (Bradbrook et al., 2000; Mahmodinia & Javan, 2021; Shen et al., 2022). The RNG k-ε model was employed to solve for the turbulent kinetic energy k and the turbulent dissipation rate ε (Yakhot & Orszag, 1986), as delineated in the subsequent formula:

$$\frac{\partial k}{\partial t} + u_j \frac{\partial k}{\partial x_j} = -u_i' u_j' \frac{\partial u_i}{\partial x_j} + \frac{\partial}{\partial x_j}\left(\frac{K_m \partial k}{\sigma_k \partial x_j}\right) - \varepsilon \tag{4}$$

$$\frac{\partial \varepsilon}{\partial t} + u_j \frac{\partial \varepsilon}{\partial x_j} = -C_{\varepsilon 1}\frac{\varepsilon}{k} u_i' u_j' \frac{\partial u_i}{\partial x_j} + \frac{\partial}{\partial x_j}\left(\frac{K_m \partial \varepsilon}{\sigma_\varepsilon \partial x_j}\right) - C_{\varepsilon 2}\frac{\varepsilon^2}{k} - R \tag{5}$$

$$K_m = v\left(1 + \left(\frac{\nu_t}{\nu}\right)^{1/2}\right)^2 \tag{6}$$

$$R = \frac{C_\mu \eta'^3 (1 - \eta'/\eta_0')\varepsilon^2}{(1 + \beta' \eta'^3) k} \tag{7}$$

$$\eta' = \frac{k}{\varepsilon}\left[\left(\frac{\partial u_i}{\partial x_j} + \frac{\partial u_j}{\partial x_i}\right)\frac{\partial u_i}{\partial x_j}\right]^{1/2} \tag{8}$$

where u_i' (m/s) is the fluctuating velocities of each direction; K_m is the time-averaged strain rate, R is the extra strain rate, η' is the dimensionless shear rate, η_0' is the fixed point value $\eta_0' = 4.38$ and coefficients $C_{\varepsilon 1}$ and $C_{\varepsilon 2}$ are constants that are usually determined from benchmark experiments and have values of 1.42 and 1.68, $C_{\varepsilon 2}$ is the power law of turbulence decay, σ_k and σ_ε are the reciprocals of the effective turbulent Prandtl number of k and ε, respectively, and both are 0.7179; and β' is an empirical constant, and its value is 0.012 (Shen et al., 2019, 2021).

Free liquid surface is captured using the Volume-of-Fluid (VOF) approach implemented within the interFoam solver. Two-phase interfacial tracking was achieved through scalar fields F_w (x, y, z, t) and F_a (x, y, z, t), representing the water and air volume fractions, respectively. The governing equation for phase fraction transport is expressed as:

$$\frac{\partial F}{\partial t} + \nabla(F u_i) = 0 \tag{9}$$

The governing equations are discretized with a finite volume method in space with a difference scheme for time. The convection terms were discretized in the non-conservation form, combining the discretization method of the central differencing scheme and the upwind scheme. The PIMPLE algorithm integrates the SIMPLE and PISO methods, boosting computational efficiency in long-time-step simulations of transient incompressible flows (Shen et al., 2023). The smoothSolver algorithm from OpenFOAM was applied to resolve the implicit matrices of

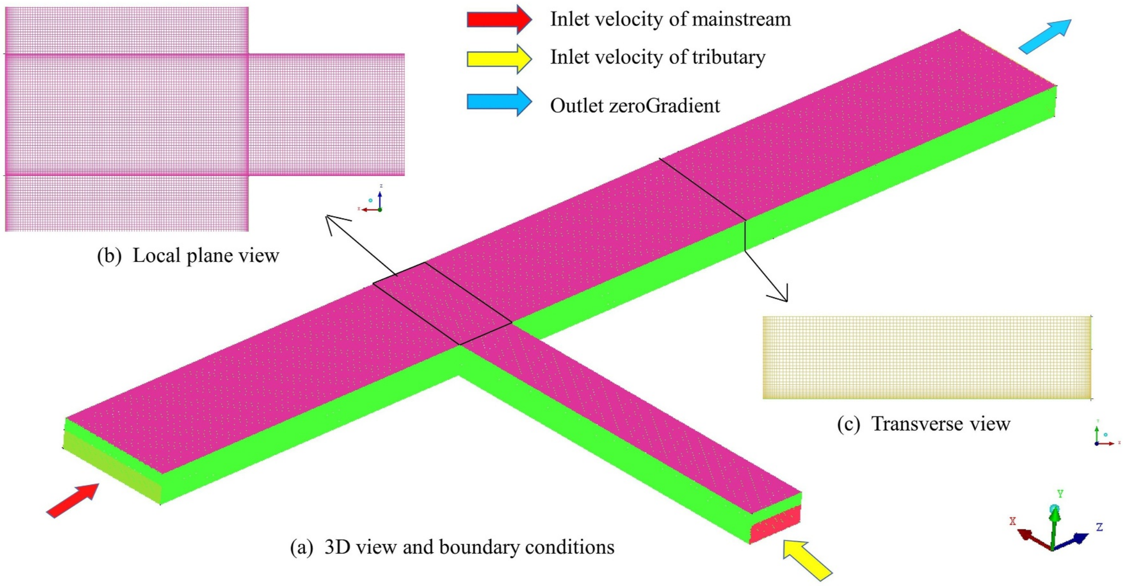

Figure 4. Domain, boundary conditions and mesh cells of the simulation.

variables, including velocity, turbulent kinetic energy, turbulent dissipation rate, and other variables. The time step adjustment was governed by the Courant number, which was kept consistently below 1 across all cases.

The boundary conditions and meshes distribution within the computational domain were set in accordance with the experimental conditions, as shown in Figure 4. The boundary conditions of the inlet in the mainstream and tributary, and outlet were fixed as velocity, velocity, and zeroGradient, respectively. The unstructured hexahedral grids were used in this numerical simulation. To ensure the calculation results effectively simulate the flow separation, finer cells were imposed near the junction and the walls. The grid dependency study was carried out with simulated velocities of the three meshes. Three meshes with cells 4 × 10 × 10 mm (coarse mesh), 2 × 10 × 10 mm (medium mesh), and 0.8 × 10 × 10 mm (fine mesh) were taken in this study. In the fine and medium mesh case, the discrepancy in the u is insignificant. However, in the case of the coarse mesh, the u shows inconsistency. Therefore, in the present study, the medium mesh size is used, and the details of the grid sensitivity analysis are presented in Appendix A.

The near-wall grid resolution (2 × 10 × 10 mm) was governed by y^+ criteria ($y^+ = 20$) in the numerical framework. A y^+ value of 20 was achieved, necessitating wall function. This approach simplifies the boundary-layer resolution by neglecting the viscous sublayer and the buffer layer, which may reduce accuracy in regions with strong flow separation, such as near the separation/recirculation zone. Despite this inherent limitation in resolving complex separated flows, the model's accuracy in capturing bulk flow features—including separation/recirculation zone size and the maximum velocity—remains acceptable for engineering applications (Shakibainia et al., 2010; Shen et al., 2022). This parametric configuration maintained a controlled maximum cell aspect ratio of 10. The numerical simulation setup parameters are comprehensively summarized in Table 2. For the wall boundary conditions, the wall function method was:

$$U^* = \begin{cases} y^* & y^* < 11.63 \\ \dfrac{1}{\kappa}\ln\left(Ey^*\right) & y^* \geq 11.63 \end{cases} \tag{10}$$

$$U^* = \frac{\mu_0 C_u^{1/4} k^{1/2}}{\tau_w/\rho}$$
$$y^* = \frac{\rho \mu_0 C_u^{1/4} k^{1/2} y}{u} \tag{11}$$

Table 2
Summary Table of Numerical Simulation Settings

Category	Parameter	Setting/Method
Solver and Algorithm	Solver	interFoam
	Algorithm	PIMPLE, PCG and smoothSolver
	Time step	Adaptive (based on Courant number)
	Max Courant Number	Below 1
Boundary condition	Inlet	Velocity
	Outlet	zoreGradient
	Wall	noSlip
	Atmosphere	zeroGradient
Turbulence model	Model type	RNG k-ε model
	Wall function	epsilonWallFunction
Discretization Schemes	Time derivatives	Euler
	Laplacian term	Gauss linear
	Gradient term	Gauss linear
	Convection Term	Gauss upwind and Gauss linear
Mesh	Mesh Type	Unstructured hexahedral
	Maximum mesh	10 × 10 × 10 mm
	Minimum mesh	2 × 10 × 10 mm
	Total number	5,660,730

where U^* and y^* are both dimensionless parameters and represent velocity and distance; κ is the Karman constant and the value is 0.41; y (m) is the distance between the node and the wall; E is the experiment constant and the value is 9.81; τ_w (N/m^2) is the wall shear stress; k (m^2/s^2) is the turbulent kinetic energy at the calculation node; and μ_0 (Pa·s) is the fluid dynamic viscosity.

3.2. Validation of the Numerical Simulations

The open-source software OpenFOAM was successfully applied in many CFD studies (Fuentes-Pérez et al., 2018; Shaheed et al., 2019). The evaluation criteria proposed by Bennett et al. (2013) were employed to assess the rationality of the numerical model, specifically using bias, relative bias, Mean Squared Error (MSE), Root Mean Squared Error, Mean Absolute Error, and Absolute Maximum Error to obtain key residual criteria. The simulation results are summarized in Table 3 and Figure 5. Figure 5 compares the experimental and simulated longitudinal velocity and depth for cases A3–A5 and B3–B5. The longitudinal flow velocity u is expressed as a dimensionless form as u/u_d, where u_d is the cross-sectional average flow velocity in the downstream branch, being $u_d = (Q_t + Q_m)/W_d H$. The numerically predicted depths were extracted at the value of the volume fraction function equal to 0.5.

It was found that the average error across different cases generally remained within 10%, with the maximum error near the bed and wall surfaces. When excluding data points near the wall and the recirculation zone boundary, the average error is less than 5%, and the maximum error is less than 10%, demonstrating the accuracy of the numerical simulations. The location of the shear layer is clearly defined by the zones of large k within CHZ (Yuan et al., 2016). Since this paper does not involve the physical analysis of the flow characteristics in the recirculation zones, the "zero-unit-discharge method" (ZUDM) was used to identify the boundary position of the recirculation zone (Jin et al., 2023; Schindfessel et al., 2017). In the ZUDM, for a specified riverbed elevation (z) and cross-sectional position (x), the local width of the horizontal recirculation zone (denoted as $W(x,z)$), is defined such that the corresponding discharge per unit height, found by integrating the lateral profile of the longitudinal velocity component (u) from the inner bank, is zero:

$$\int_0^{W(x,z)} u(x,y,z)\,dy = 0 \tag{12}$$

Table 3
Key Residual Criteria and Results of the Longitudinal Flow Velocity and Water Depth of the Numerical Models

				90		60	
Method name	Formula	Range	Ideal value	Velocity	Depth	Velocity	Depth
Bias	$\frac{1}{n}\sum_{i=1}^{n}(y_i - \overline{y_i})$	$(-\infty, +\infty)$	0	0.0329 m/s	−0.0034 m	−0.0328 m/s	0.0022 m
Relative bias	$\frac{1}{n}\sum_{i=1}^{n}(y_i - \overline{y_i})/\overline{y_i}$	$(-1, 1)$	0	0.0501	−0.0099	−0.0287	−0.0055
MSE	$\frac{1}{n}\sum_{i=1}^{n}(y_i - \overline{y_i})^2$	$(0, +\infty)$	0	0.0046 m/s	0.0002 m	0.0056 m/s	0.0002 m
RMSE	$\sqrt{\frac{1}{n}\sum_{i=1}^{n}(y_i - \overline{y_i})^2}$	$(0, +\infty)$	0	0.066 m/s	0.0128 m	0.0725 m/s	0.0142 m
MAE	$\frac{1}{n}\sum_{i=1}^{n}\lvert y_i - \overline{y_i}\rvert$	$(0, +\infty)$	0	0.0567 m/s	0.0119 m	0.0635 m/s	0.0114 m
AME	$\max\lvert y_i - \overline{y_i}\rvert$	$(0, +\infty)$	0	0.1711 m/s	0.0121 m	0.1459 m/s	0.0108 m

4. Results

4.1. The Impact of the Shear Layer on Longitudinal Flow Velocity

Due to the velocity differences between the main channel and the tributary, a shear layer consisting of quasi-two-dimensional vortices with near vertical axes is formed, as illustrated in Figure 6a. The mixing process at river confluences follows two modes: wake mode and mixing-layer mode (Sukhodolov et al., 2023). During its

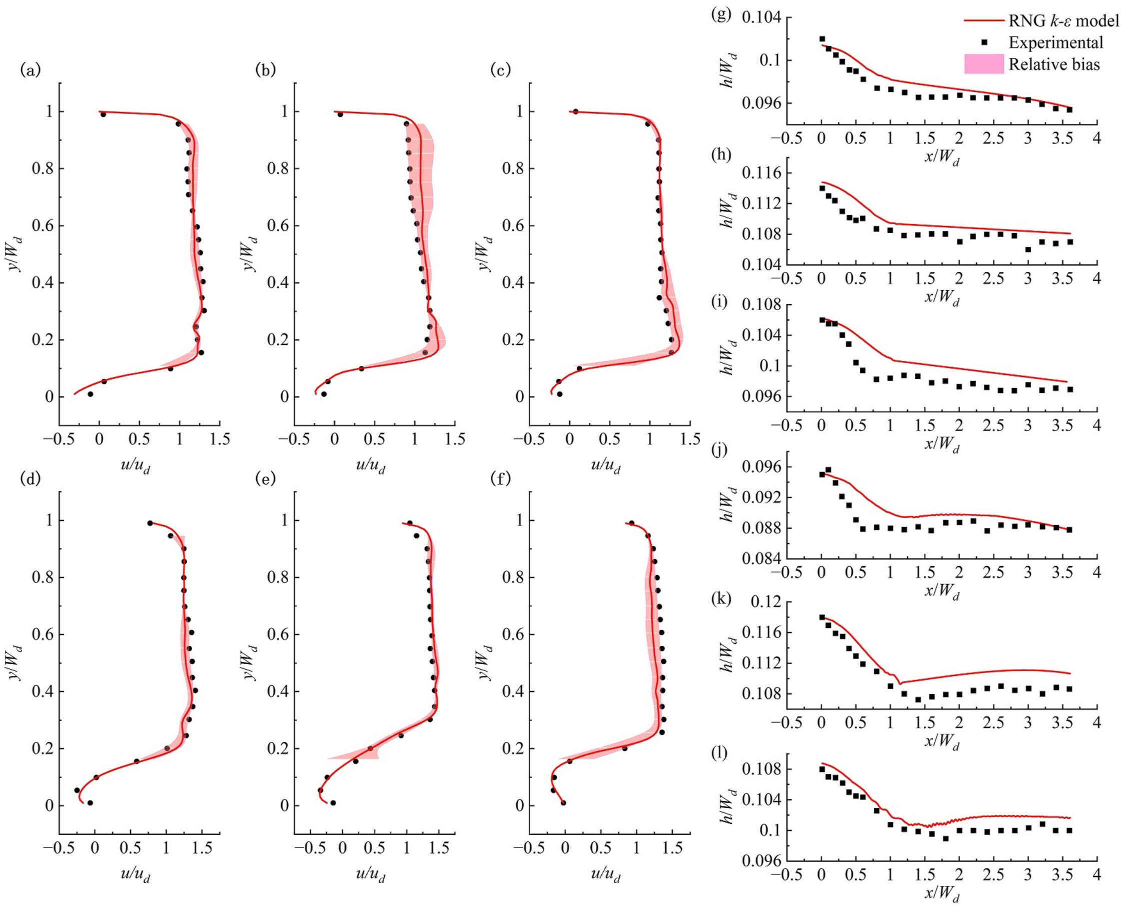

Figure 5. Comparison between numerical results and experimental data. (a–f) The lateral distribution of the dimensionless longitudinal velocity at $z = 0.06$ m at I. (a) case A3, (b) case A4, (c) case A5, (d) case B3, (e) case B4, (f) case B5. (g–l) Distribution of water surface elevation at $y = 0.5$ m. (g) case A3, (h) case A4, (i) case A5, (j) case B3, (k) case B4, (l) case B5.

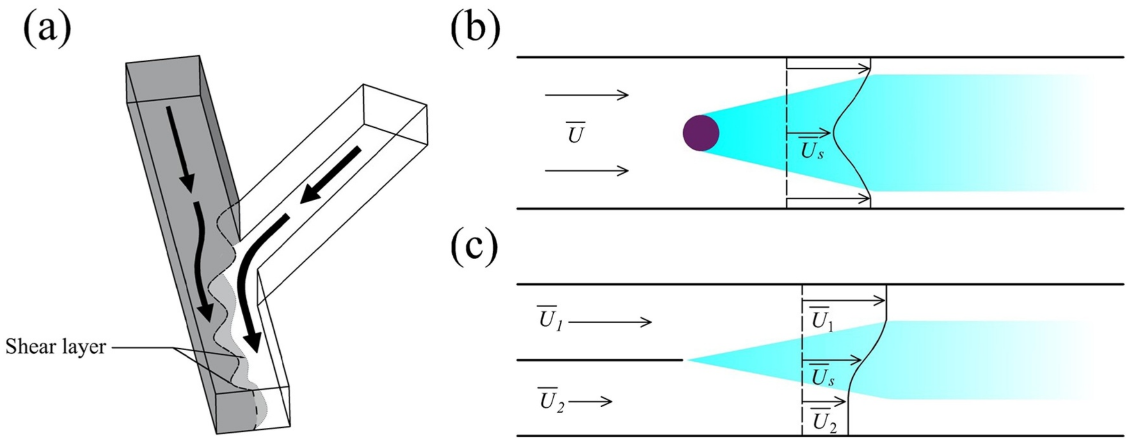

Figure 6. (a) Conceptual diagrams showing modes of the shear layer at the confluences; type of shear layer: (b) wake and (c) mixing-layer (adapted from Rhoads & Sukhodolov, 2008).

formation, the shear layer exhibits wake mode and transitions to mixing-layer mode as it progresses downstream. Miyawaki et al. (2009, 2010) demonstrate that an increase in M_r from 1 to 5 induces a change in the mixing-layer structure from the wake mode to the mixing-layer mode driven by the Kelvin-Helmholtz instability.

In the wake mode, the average velocity within the shear layer is lower than the velocities on either side (Rhoads & Sukhodolov, 2008), as illustrated in Figure 6b and the shear layer divides the contracted flow into two parts: the main channel inflow and the tributary channel inflow. Therefore, it can be assumed that the line connecting the minimum flow velocity positions within the shear layer at each cross-section represents the hypothetical interface between the main channel inflow and the tributary channel inflow in the contraction section. The hypothetical interface divides the contraction section flow into two control volumes, as shown in Figure 6a, V_1 and V_2, which represent the main channel inflow and the tributary channel inflow, respectively. Figure 7 shows the hypothetical interface's position for some cases, represented by the dimensionless number W_1/W_d, where W_1 is the width in V_1. Figure 7 illustrates that, with a constant θ, the value of W_1/W_d decreases as η increases. For the same η, a larger θ results in the hypothetical interface being situated closer to the outer bank. The wall of the main channel connected to the tributary is defined as the inner bank, and its opposite side is defined as the outer bank. It is evident that the hypothetical interface's position shifts toward the outer bank as M_r increases. This is consistent with the findings in natural channels of Kenworthy and Rhoads (1995) and Gualtieri et al. (2019).

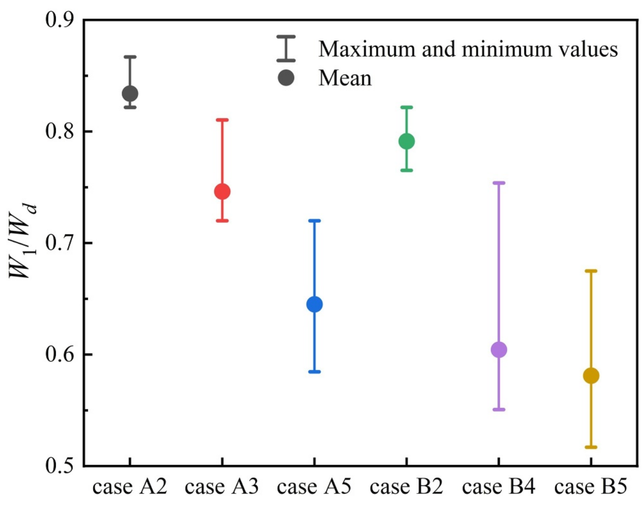

Figure 7. Diagram of boundary line positions for the cases A2, A3, A5, B2, B4, and B5.

When the shear layer is in the wake mode, significant velocity lateral gradients exist inside the shear layer (Rhoads & Sukhodolov, 2008) and the Reynolds shear stress $<u'v'>$ within the shear layer is substantially higher than outside it (Yuan et al., 2016), resulting in two velocity peaks distributed on either side of the shear layer within the effective flow cross-section of the contracted flow section (Rhoads & Sukhodolov, 2001; Shakibainia et al., 2010), as shown in Figures 8 and 9. The control volume V_1, which is influenced by both the shear stress from the wall and the shear layer, forms the maximum velocity between the shear layer and the outer bank wall. Similarly, the control volume V_2, which is influenced by the shear stress from the recirculation zone and the shear layer, forms the maximum velocity between the boundary of the recirculation zone and the shear layer. Figure 10a shows a sketch of V_1 and V_2 and the associated shear stress distribution.

When the shear layer transitions to the mixing-layer mode, as shown in Figure 6c, there is a single velocity peak along the horizontal measurement line, and a velocity gradient exists within the shear layer from the high-velocity control volume to the low-velocity control volume. Initially, as the flow enters the contracted section, it is divided into two parts by the shear layer in the wake mode, as illustrated in Figures 11b and 12b. However, as the

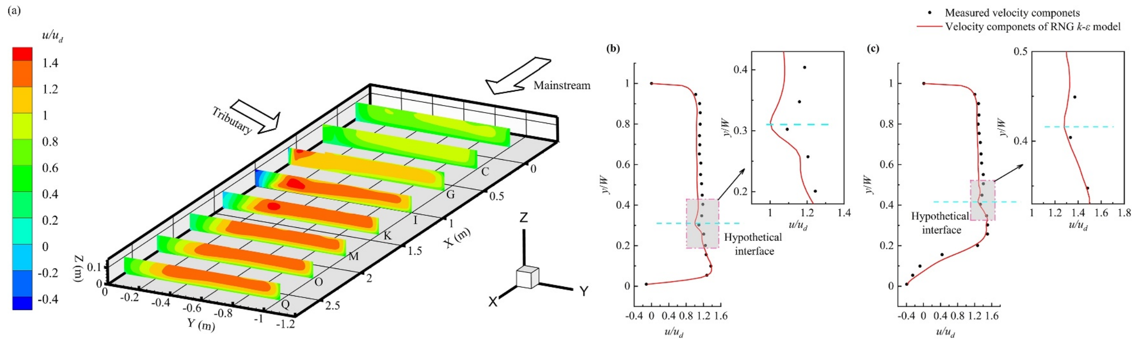

Figure 8. In case A5, the schematic diagram of longitudinal flow velocity at specific cross-sections shows (a) Contours of flow velocity distribution (b) Water surface elevation $z = 0.101$ m, G section, and (c) Water surface elevation $z = 0.101$ m, I section.

flow progresses downstream, the wake mode shifts into the mixing-layer mode, and the flow in the contraction section is studied using a single control volume V_3, the sketch of V_3 is shown in Figure 10b. This control volume is influenced by shear stress from the wall and the recirculation zone, resulting in a single velocity peak within the control volume, as illustrated in Figures 11c and 12c.

4.2. The Impact of the Recirculation Zone on the Longitudinal Flow Velocity

The dimensionless maximum velocity u_{max}/u_d in each case is presented in Figure 13a. Figure 13a shows that as η increases, u_{max}/u_d also increases. This is because a higher η results in a larger recirculation zone, reducing the effective flow cross-section area and thus increasing the flow velocity (Schindfessel et al., 2015). The region of maximum flow velocity occurs within the contraction zone formed by the boundary of the recirculation zone and the opposing wall (Jin et al., 2023; Shakibainia et al., 2010). Figure 13b indicates that changes in u_d, under a constant η, have negligible effects on u_{max}/u_d, with the primary influence on u_{max} alterations stemming from compression within the recirculation zone. The largest contraction was found for the minimum cross-sectional area, that is, for the widest recirculation zone. The maximum width of the recirculation zone is observed near the water surface (Shakibainia et al., 2010), and the bed shear stresses exerted by bed friction are also at their lowest. Consequently, it is posited that u_{max} closely approximates the peak velocity observed at the cross-section of the maximum recirculation zone width. Figure 14 illustrates the relationship between u_{max} and the maximum flow velocity $u_{max,re}$ at the cross-section where the recirculation zone width is greatest. As shown in Figure 14, u_{max} and $u_{max,re}$ are closely matched. Their deviation is quantitatively described using the relative error and the absolute error.

$$\varepsilon_u = \frac{|u_{max,re} - u_{max}|}{u_{max}} \times 100\% \tag{13}$$

The absolute error is given as:

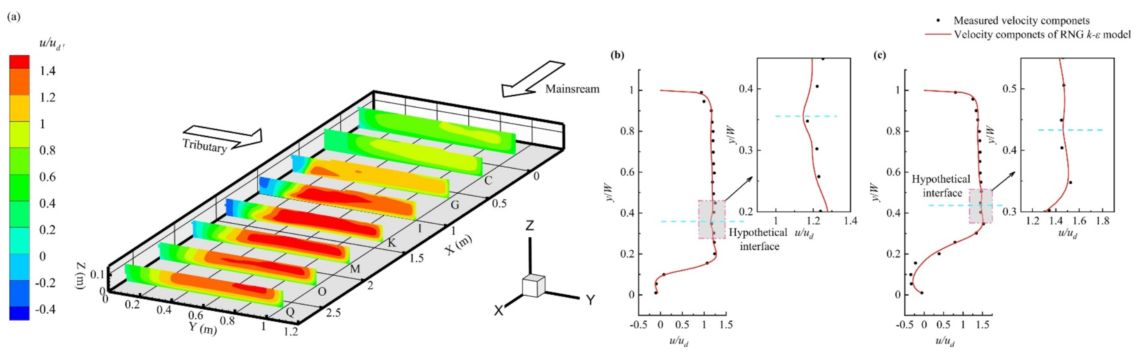

Figure 9. In case B5, the schematic diagram of longitudinal flow velocity at specific cross-sections shows (a) Contours of flow velocity distribution (b) Water surface elevation $z = 0.106$ m, G section, and (c) Water surface elevation $z = 0.106$ m, I section.

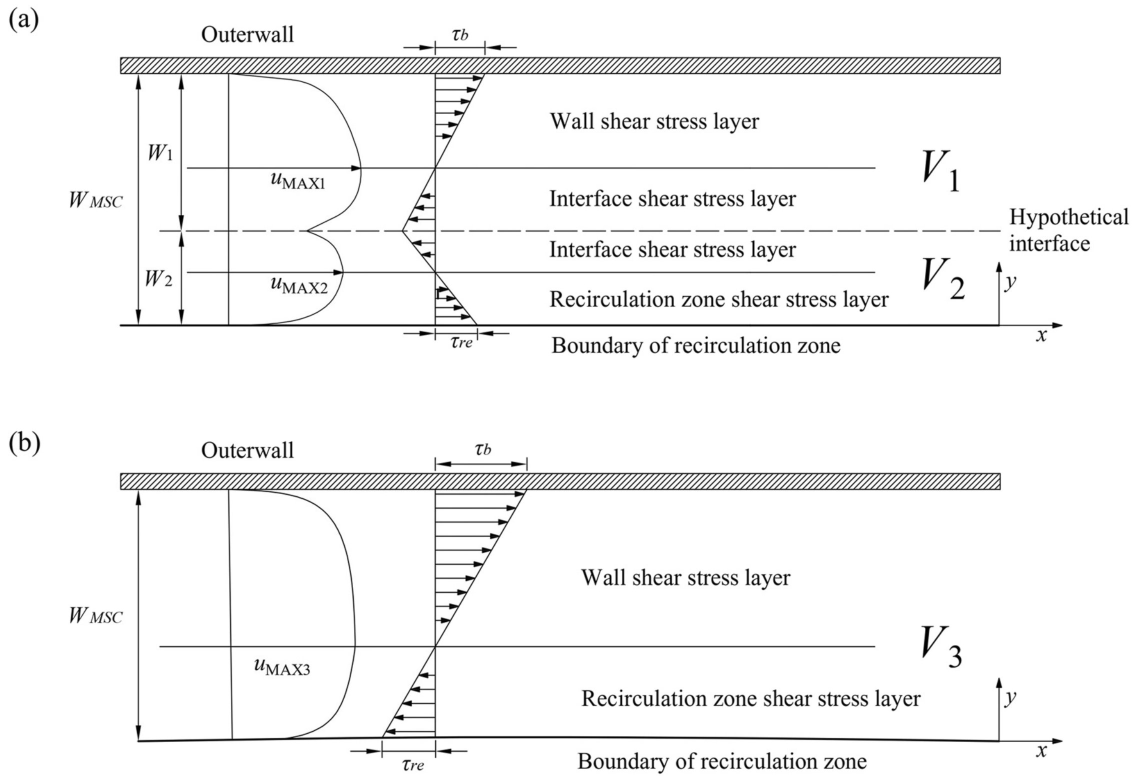

Figure 10. Sketch of control volume, (a) the shear layer in the wake mode; (b) the shear layer in the mixing-layer mode.

$$\varepsilon_e = |u_{\max,\mathrm{re}} - u_{\max}| \tag{14}$$

Tables 4 and 5 present the results for junction angles of 90° and 60°, respectively. The maximum absolute error between $u_{\max}$ and $u_{\max,\mathrm{re}}$ was observed for Case B6, with a value of 0.0256 m/s, while all cases maintain errors below 5%. Thus, $u_{\max,\mathrm{re}}$ can be used as an estimate for $u_{\max}$. For a 90° junction angle, the ε_e and ε_u values were generally higher than those for the 60° junction angle. Additionally, as η increased, the deviation between $u_{\max}$ and $u_{\max,\mathrm{re}}$ also increased, suggesting that as the proportion of transverse momentum increased, the deviation between $u_{\max}$ and $u_{\max,\mathrm{re}}$ continued to grow.

Although the values of $u_{\max}$ and $u_{\max,\mathrm{re}}$ are very similar, this does not necessarily imply that $u_{\max}$ occurs at the widest cross-section of the recirculation zone or free surface, because the velocity-dip phenomenon often causes

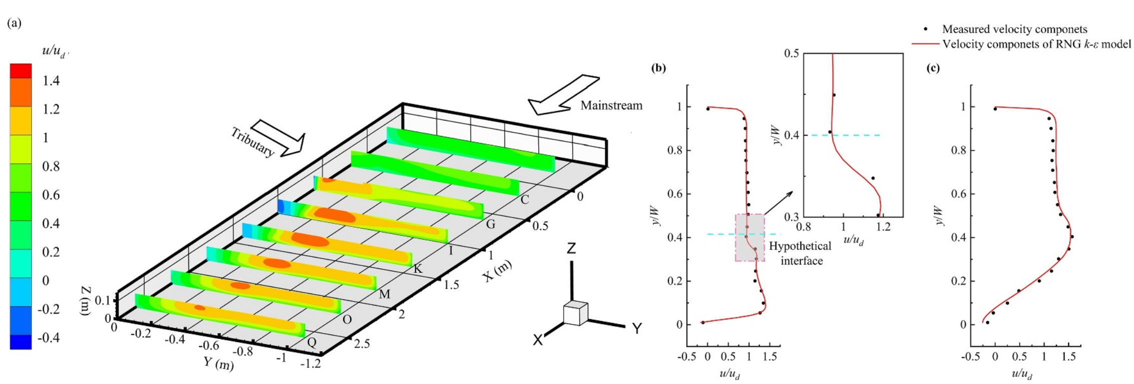

Figure 11. In case A7, the schematic diagram of longitudinal flow velocity at specific cross-sections shows (a) Contours of flow velocity distribution (b) Water surface elevation $z = 0.073$ m, G section, and (c) Water surface elevation $z = 0.073$ m, K section.

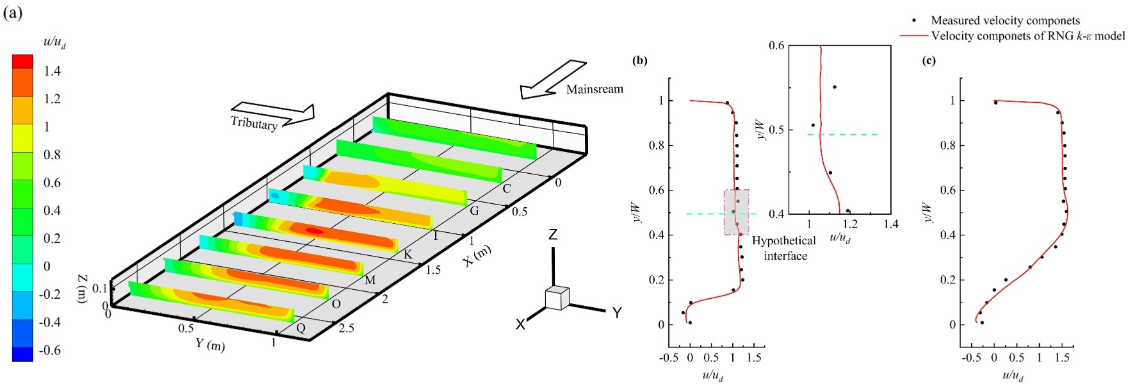

Figure 12. In case B7, the schematic diagram of longitudinal flow velocity at specific cross-sections shows (a) Contours of flow velocity distribution (b) Water surface elevation $z = 0.073$ m, G section, and (c) Water surface elevation $z = 0.073$ m, K section.

$u_{\max}$ to occur below the free surface (Yuan et al., 2024). According to the current simulation results, in case A5 the largest longitudinal offset is 0.4 m, whereas in case B7 the largest vertical offset is 0.03 m. However, this does not affect the application of the assumption in subsequent derivations, since the assumption prioritizes velocity magnitude over precise positional accuracy.

5. Calculation of the Maximum Flow Velocity

The formation of the recirculation zone reduces the effective flow area, causing the flow to accelerate, and $u_{\max,\mathrm{re}}$ can be used as an estimate for $u_{\max}$. Therefore, before deriving the expression for the maximum flow velocity, it is necessary to calculate the maximum width of the recirculation zone at the water surface and the position of the hypothetical interface. The derivation process for the surface recirculation zone width is provided in Appendix B.

5.1. Calculation of the Maximum Longitudinal Flow Velocity

5.1.1. Calculation of the Maximum Velocity Influenced by the Shear Layer in the Wake Mode

The position of the shear layer is predominantly governed by M_r (Boyer et al., 2006; De Serres et al., 1999; Jiang et al., 2023), thereby yielding an expression for the hypothetical interface location as follows:

$$\frac{W_2}{W_1} = \frac{Q_{\mathrm{TUS}} \cdot \sin(\theta)}{Q_{\mathrm{TUS}} \cdot \cos(\theta) + Q_{\mathrm{MUS}}} + \varphi \tag{15}$$

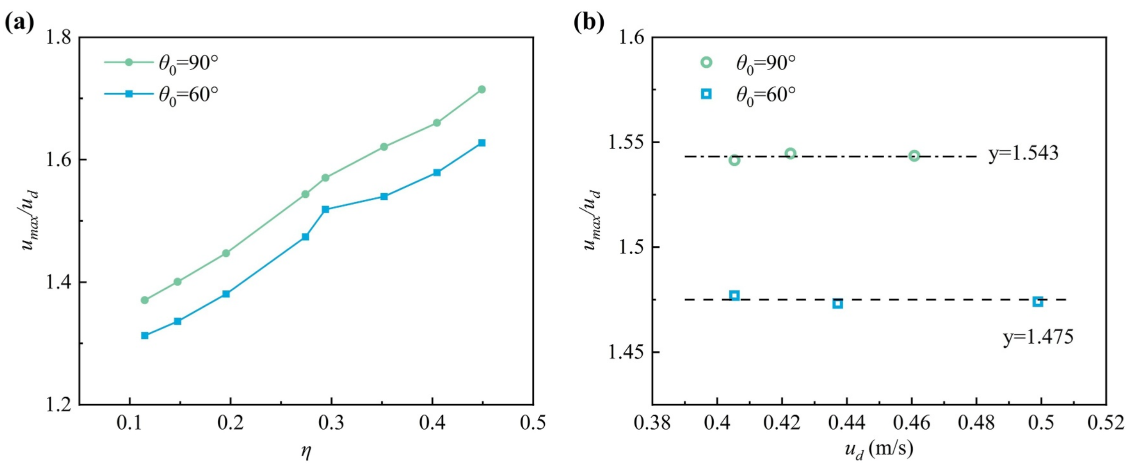

Figure 13. Schematic diagram of the maximum flow velocity variation derived from simulations. (a) The maximum flow velocities in Cases A1–A8 and B1–B8. (b) The maximum flow velocities for Cases A4, A9, A10, B4, B9, and B10.

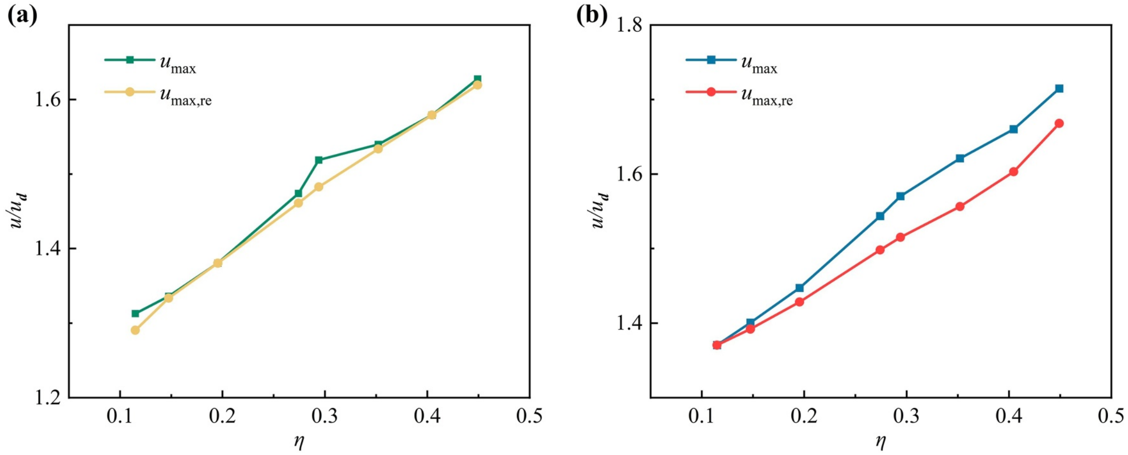

Figure 14. The maximum longitudinal flow velocity u_{max} within the confluence versus the maximum cross-sectional flow velocity $u_{max,re}$ at the largest width of the recirculation zone. (a) Cases at a 60° junction angle; (b) Cases at a 90° junction angle.

where φ is an empirical coefficient delineating the impact of secondary flows on the hypothetical interface's position, calibrated as 0.02 through simulated results; W_2 is the effective cross-sectional width of the flow for V_2, in the previous section, it was mentioned that u_{max} is similar to $u_{max,re}$, then it follows that $W_1 + W_2 = W_{MCS}$. Shear stress arising at the interface due to velocity gradients between the shear layer and adjacent control volumes acts upon V_1 and V_2. This shear stress acts on both control volumes, oriented inversely to the flow direction, with its magnitude approximately delineated as (Shabayek et al., 2002):

$$\tau_{sh} = \rho\left(\frac{f_{sh}}{8}\right)\left|u_1^2 - u_2^2\right| \tag{16}$$

where τ_{sh} is the shear force exerted on the control volume at the interface; f_{sh} is the hypothetical interface shear coefficient, the derivation is provided in Appendix C; u_1 and u_2 are the average flow velocities across cross-sections of V_1 and V_2, respectively. In accordance with the mass conservation equation, the average flow velocities u_1 and u_2 in V_1 and V_2 are expressed as

$$\begin{aligned} u_1 &= \frac{Q_{MUS}}{\Delta h W_1} = \frac{u_{MUS}\Delta h_{MUS} W_{MUS}}{\Delta h_{MSC} W_1} \\ u_2 &= \frac{Q_{TUS}}{\Delta h W_2} = \frac{u_{TUS}\Delta h_{TUS} W_{TUS}}{\Delta h_{MSC} W_2} \end{aligned} \tag{17}$$

The control volume V_1 is subjected to the combined effects of shear forces from the wall and shear forces from the hypothetical interface. The sheer force τ_b on V_1, induced by wall friction, can be expressed as:

$$\tau_b = \rho\left(\frac{f_b}{8}\right) u_1^2 \tag{18}$$

where f_b is the Darcy–Weisbach friction factor of the wall, the derivation is provided in Appendix C; τ_b is the boundary shear stress exerted by the wall on V_1. Regarding V_2, a lateral shear stress τ_{re} aligned with the direction

Table 4
Error Between u_{max} and $u_{max,re}$ for Different Cases at a 60° Junction Angle

Case	A1	A2	A3	A4	A5	A6	A7	A8	A9	A10
ε_e (m/s)	0.0116	0.0011	0	0.0065	0.0165	0.0024	0.0002	0.0035	0	0.002
ε_u (%)	1.7	0.17	0	0.88	2.37	0.39	0.03	0.49	0	0.31

Table 5
Error Between u_{max} and $u_{max,re}$ for Different Cases at a 90° Junction Angle

Case	B1	B2	B3	B4	B5	B6	B7	B8	B9	B10
ε_e (m/s)	0.0001	0.0042	0.0083	0.0254	0.0242	0.0256	0.0242	0.0204	0.0213	0.02
ε_u (%)	0.01	0.62	1.3	3.56	3.51	3.98	3.44	2.73	3.42	3.07

of water flow exists at the boundary of the recirculation zone. τ_{re} is calculated in a similar way to τ_{sh}. The shear stress τ_{re} imposed on V_2 by the recirculation zone is defined as:

$$\tau_{\text{re}} = \rho\left(\frac{f_{\text{re}}}{8}\right)u_2^2 \tag{19}$$

where f_{re} is the recirculation zone shear coefficient, the derivation is provided in Appendix C. Consequently, V_2 is subjected to the combined influence of τ_{re} and τ_{sh}.

As depicted in Figure 15, a Cartesian coordinate system was established with its origin positioned at the boundary of the recirculation zone; the x-axis runs parallel to the main channel wall, while the y-axis is perpendicular to the tangent at the boundary of the maximum width of the recirculation zone. Within V_1, τ_b and τ_{sh} act in opposing directions, mirroring shear stress conditions found in asymmetric channels (Tsai & Ettema, 1994). Following Einstein's theory of drag separation (Einstein, 1942), V_1 is bisected into two layers by the zero-shear stress position: one influenced by wall shear stress and the other by hypothetical interface shear stress, assuming shear forces are linearly varying, as shown in Figure 10a. Similarly, in V_2, the shear stress from the recirculation zone opposes that from the hypothetical interface, partitioning V_2 into layers, namely, the interface shear stress layer and the recirculation zone shear stress layer. The lateral shear stresses in V_1 and V_2 are defined as:

$$\begin{aligned}\tau_{V_1} &= \tau_b - (\tau_b + \tau_{\text{sh}})\,\frac{W_1 + W_2\ - y}{W_1}\\ \tau_{V_2} &= \tau_{\text{re}} - (\tau_{\text{re}} + \tau_{\text{sh}})\,\frac{y}{W_2}\end{aligned} \tag{20}$$

In each control volume, it is assumed that the positions where the shear stresses, τ_{V_1} and τ_{V_2} are zero coincide with the locations of maximum flow velocity within the control volume. Consequently, by substituting $\tau_V\ = 0$ into Equation 20, the positions of maximum flow velocity in V_1 and V_2 are expressed as:

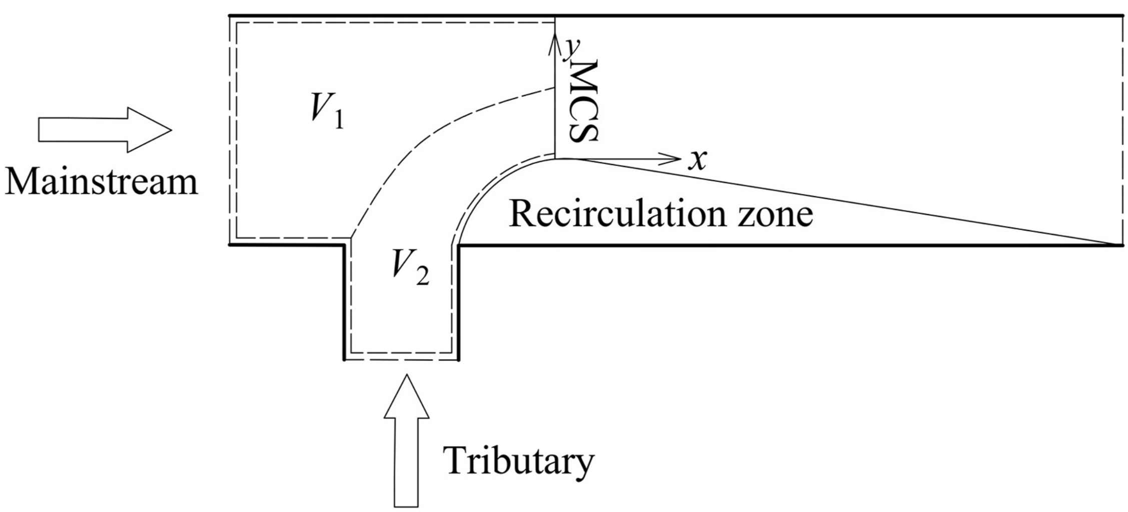

Figure 15. Sketch of the Cartesian coordinate system with the x-axis and y-axis.

$$y_1' = W_1 + W_2 - \frac{\tau_b}{\tau_b + \tau_{sh}} W_1$$
$$y_2' = \frac{\tau_{re}}{\tau_{re} + \tau_{sh}} W_2 \tag{21}$$

By substituting Equation 21 into Equation 20, the expression for the shear stress in the wall shear stress layer of V_1 and the shear stress in the recirculation zone shear stress layer of V_2 are derived as:

$$\tau_{V_1} = \tau_b \left(1 - \frac{W_1 + W_2 - y}{W_1 + W_2 - y_1'}\right)$$
$$\tau_{V_2} = \tau_{re} \left(1 - \frac{y}{y_2'}\right) \tag{22}$$

Based on the mixing length theory, the turbulent time-averaged shear stress within the shear stress layer of the control volume, when turbulence is fully developed, is expressed as:

$$\tau = \rho l^2 \left(\frac{du}{dy}\right)^2 \tag{23}$$

In the wall shear stress layer of V_1 and the separated shear layer of V_2, the mixing lengths are expressed as:

$$l_b = \kappa (W_1 + W_2 - y) \sqrt{1 - \frac{W_1 + W_2 - y}{W_1 + W_2 - y_1'}}$$
$$l_{re,V_2} = \kappa y \sqrt{1 - \frac{y}{W_2}} \tag{24}$$

By substituting Equations 16, 18, 20, and 24 into Equation 23, and setting $y = y_1{}'$ the expression for the maximum flow velocity within the V_1 is derived as:

$$u_{max1} = \frac{u_1}{\kappa} \sqrt{\frac{f_b}{8}} \ln \frac{f_b u_1^2}{f_b u_1^2 + f_{sh} |u_1^2 - u_2^2|} W_1 + C_1 \tag{25}$$

Similarly, by substituting Equations 16, 19, 22, and 24 into Equation 23 and setting $y = y_2{}'$, the expression for the maximum flow velocity within the V_2 is derived as:

$$u_{max2} = \frac{u_2}{\kappa} \sqrt{\frac{f_{re}}{8}} \ln \frac{f_{re} u_2^2}{f_{re} u_2^2 + f_{sh} |u_1^2 - u_2^2|} W_2 + C_2 \tag{26}$$

5.1.2. Calculation of the Maximum Velocity Influenced by the Shear Layer in the Mixing-Layer Mode

At the shear layer in the mixing-layer mode, the contracted flow is considered as a single control volume, influenced solely by the transverse shear stress from the recirculation zone and walls, as shown in Figure 10b. The shear stress τ_{re} and τ_b within V_3 are then expressed as:

$$\tau_{V_3} = \tau_{re} - (\tau_{re} + \tau_b) \frac{y}{W_3} \tag{27}$$

In V_3, when the lateral shear force is zero, that is, $\tau_{V_3} = 0$, it indicates the position of maximum longitudinal flow velocity. Therefore, the position of maximum flow velocity within V_3 is represented as:

$$y_3' = \frac{\tau_{re}}{\tau_{re} + \tau_b} W_3 \tag{28}$$

Table 6
Parameter Statistics Table for the 60° Cases

Case	A1	A2	A3	A4	A5	A6	A7	A8	A9	A10
Model	Mixing-layer model	Wake model	Wake model	Mixing-layer model	Wake model	Mixing-layer model	Mixing-layer model	Mixing-layer model	Mixing-layer model	Mixing-layer model
n_b	0.0083	0.0083	0.0083	0.0083	0.0083	0.0083	0.0083	0.0083	0.0083	0.0083
n_{re}	0.0046	0.0083	0.0041	0.0056	0.0204	0.0058	0.008	0.0068	0.0045	0.0038
n_{sh}	/	0.0037	0.0044	/	0.0041	/	/	/	/	/

The control volume V_3 is divided into the wall shear stress layer and the recirculation zone shear stress layer by the zero shear stress plane. The expression for the lateral shear stress in the recirculation zone shear stress layer is given as:

$$\tau_{V_3} = \tau_{re}\left(1 - \frac{y}{y_3'}\right) \tag{29}$$

The expression for the mixing length in the recirculation zone shear stress layer is given as:

$$l_{re,V_3} = \kappa y\sqrt{1 - \frac{y}{y_3'}} \tag{30}$$

By substituting Equations 18, 19, 27, and 30 into Equation 23, and setting $y = y_3'$, the expression for the maximum flow velocity within V_3 is derived as:

$$u_{max3} = \frac{u_3}{\kappa}\sqrt{\frac{f_{re,V_3}}{8}}\ln\frac{f_{re,V_3}u_3^2}{f_{re,V_3}u_3^2 + f_b u_3^2}W_3 + C_3 \tag{31}$$

5.2. Integration Constant

To obtain solutions for the semi-analytical models, suitable boundary conditions must be applied to the unknowns in the equations. The integration constant C_1–C_3 can be determined by substituting the flow velocity at any position within the control volume. For the computational results presented in Section 6, boundary conditions were defined at the centroids of the effective flow cross-sections at maximum recirculation zone width positions within each control volume. These positions were determined using Equation 15 combined with Equation B5, while requisite velocity data were experimentally acquired.

6. Models Validation

To validate the effectiveness and reliability of the proposed models, the results calculated by the models were compared to the simulated results. The parameters required for the calculations are presented in Tables 6 and 7. n_{re} and n_{sh} can be determined using data from any horizontal cross-section within the flow contraction zone.

Table 7
Parameter Statistics Table for the 90° Cases

Case	B1	B2	B3	B4	B5	B6	B7	B8	B9	B10
Model	Mixing-layer model	Wake model	Mixing-layer model	Wake model	Wake model	Mixing-layer model	Mixing-layer model	Mixing-layer model	Mixing-layer model	Mixing-layer model
n_b	0.0083	0.0083	0.0083	0.0083	0.0083	0.0083	0.0083	0.0083	0.0083	0.0083
n_{re}	0.0051	0.0215	0.0072	0.0107	0.0191	0.0081	0.0083	0.0085	0.0075	0.0073
n_{sh}	/	0.0081	/	0.0062	0.0059	/	/	/	/	/

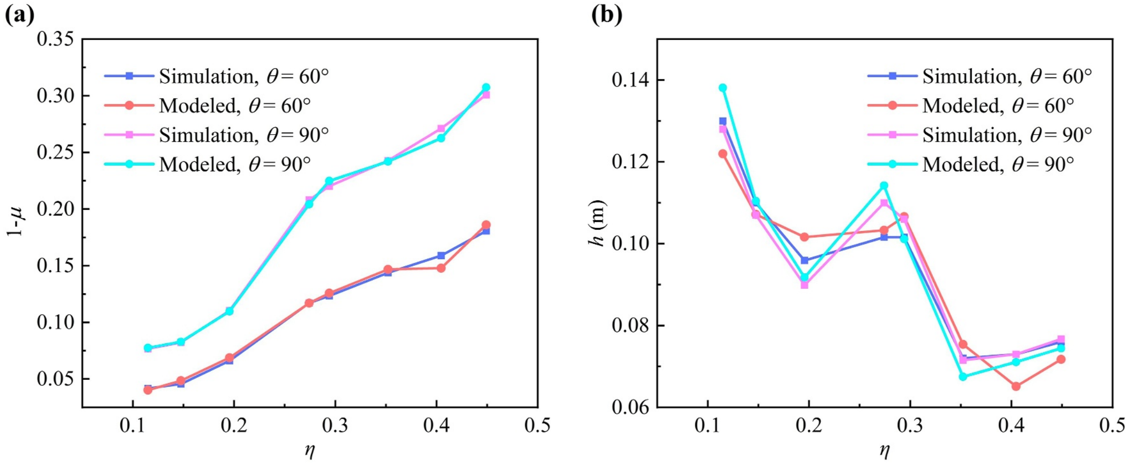

Figure 16. Comparison of model predictions versus numerical simulations, (a) Equation B5, (b) Equation B6.

As shown in Tables 6 and 7, n_{re} and n_{sh} are not constant. Specifically, n_{re} exhibits considerable variability, whereas n_{sh} remains relatively stable. Assuming that roughness reflects the influence of turbulent structures, the presence of intense turbulence near the recirculation zone boundary and within the shear layer—where large-scale vortices are convected in pairs (Rhoads & Sukhodolov, 2001, 2004; Sukhodolov & Rhoads, 2001)—may account for the observed variations in these apparent roughness values. For cases where the shear layer exhibits wake-mode behavior, the values of n_{re} are typically larger than those under mixed-mode conditions. This is because the strength of large-scale turbulent structures along the boundary of the recirculation zone diminishes downstream, and wake-mode shear layers predominantly form closer to the upstream region. In mixed-mode scenarios, for a given discharge ratio, n_{re} tends to be larger at a 90° confluence angle compared to a 60° angle. This difference may be attributed to the larger and more intense recirculation zone associated with larger confluence angles (e.g., 90° vs. 60°). These larger recirculation zones are associated with stronger adverse pressure gradients and more pronounced flow reversal, leading to increased turbulence production at their boundaries.

Before validating the maximum flow velocity, the accuracy of Equation B5 (maximum recirculation zone width at the surface) and Equation B6 (MCS water depth) must first be verified. Figures 16a and 16b provide comparative plots of the calculated versus simulated results for Equations B5 and B6, respectively.

Equation B5 demonstrates a maximum relative error of 6.9% in Case A7, with a concurrent maximum absolute deviation of 0.011. Equation B6, however, shows a higher maximum relative error (10.8%, Case A7), while its peak absolute deviation (0.01 m) occurs in Case B1. Critically, both equations maintain relative errors below 5% across most cases, validating their robustness.

The error analysis is presented in Tables 8 and 9. The absolute error ranged from 0.0002 m/s to 0.0474 m/s, with the highest value for Case B10. The range of relative errors spans from 0.05% to 7.26%. Case A9 had the highest accuracy. From an error analysis perspective, the present models can predict the maximum longitudinal flow velocity in the confluence channels with 60° and 90° junction angles.

As shown in Figure 17, the deviation exists between the predicted values and the actual values. There is mass exchange between the recirculation zone boundary and the contracted flow, as well as through the shear layer between control volumes, causing deviations in u_{max} obtained from models compared to simulations.

Table 8
Error Statistics of the Longitudinal Maximum Velocity for the Case of a 60° Junction Angle

Case	A1	A2	A3	A4	A5	A6	A7	A8	A9	A10
ε_a (m/s)	0.0106	0.0168	0.0066	0.0229	0.0194	0.0077	0.0179	0.0021	0.0002	0.0087
ε_r (%)	1.55	2.62	1.15	3.11	2.78	1.26	2.67	0.29	0.05	1.35

Table 9
Error Statistics of the Longitudinal Maximum Velocity for the Case of a 90° Junction Angle

Case	B1	B2	B3	B4	B5	B6	B7	B8	B9	B10
ε_a (m/s)	0.0077	0.0198	0.02	0.0324	0.01454	0.025	0.0174	0.0251	0.0331	0.0474
ε_r (%)	1.07	2.86	3.12	4.53	2.1	2.55	2.49	3.36	5.3	7.26

Additionally, the secondary flows in the flume affect longitudinal flow velocity (Lane et al., 2000; Pein et al., 2018). This study only considered the impact of secondary flow on the interface position. Song et al. (2012) established a two-dimensional numerical model to quantify the strength of secondary flows in the confluence channel, achieving good agreement between the calculated water surface profile and depth-averaged flow velocity with actual data. Quantifying the strength of secondary flows in the confluence channel can help improve the accuracy of $u_{\max}$.

The selection of boundary conditions for solving integration constants C_1–C_3 influences model accuracy. In this study, the velocity at the centroid of the effective flow cross-section within each control volume was selected as the boundary condition, which may account for the relatively large errors observed in the computational results. Positioning boundary conditions closer to the hypothetical interface or maximum velocity locations enhances model precision.

7. Discussion

This study proposes semi-analytical models to calculate $u_{\max}$ using the control volume method. The semi-empirical equation proposed in this study offers significantly improved computational efficiency compared to numerical models. Most notably, the equation eliminates the need for mesh generation in the model, thereby reducing setup time and ensuring the accuracy is independent of mesh properties such as size and shape. In many engineering applications, simulating the full three-dimensional flow field of the channel is unnecessary; instead, the focus lies on extreme hydraulic parameters such as the maximum flow velocity or maximum width of the separation/recirculation zone. Under these scenarios, the proposed semi-empirical equation enables rapid estimation of the maximum velocity. Furthermore, the mathematical model developed in this study can be integrated with established pollutant transport models to estimate the maximum downstream travel distance of pollutants (Zhou et al., 2023).

The semi-analytical models do not directly calculate $u_{\max}$, but they target $u_{\max,\text{re}}$, which is proximate to $u_{\max}$. This approach addresses the difficulty of capturing the exact location of $u_{\max}$, making it possible to calculate $u_{\max}$.

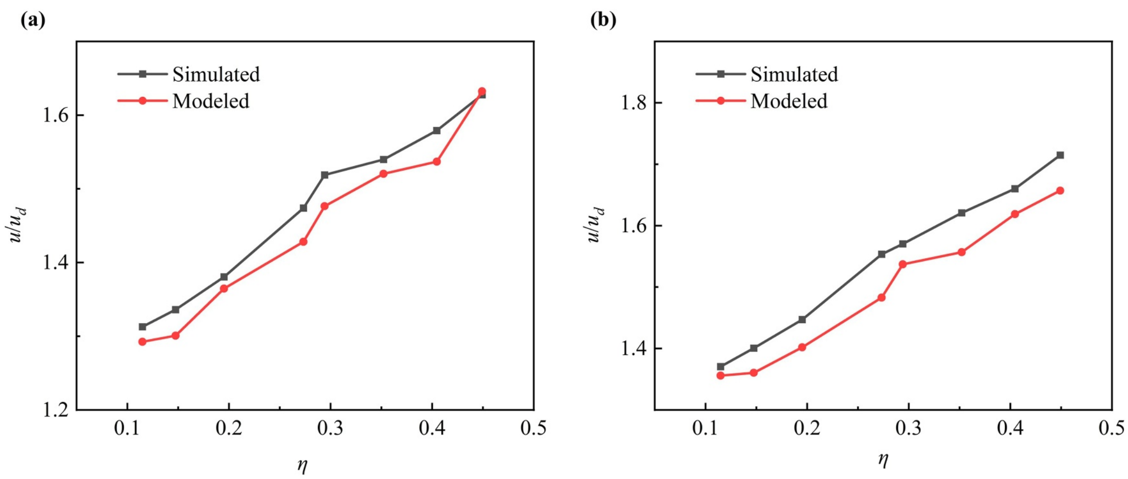

Figure 17. Comparison of the maximum longitudinal flow velocity predicted by the proposed models with the simulation. (a) Cases at a 60° junction angle. (b) Cases at a 90° junction angle.

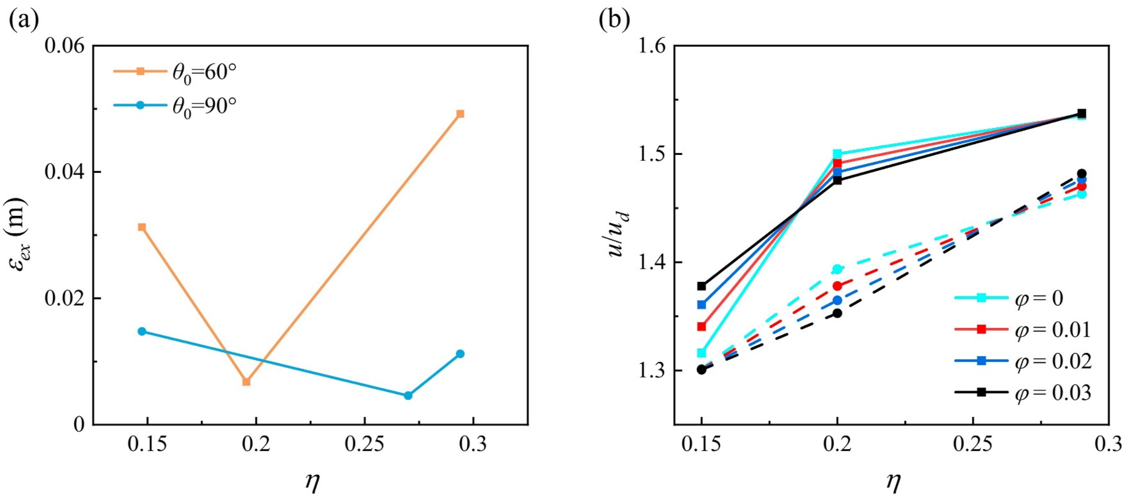

Figure 18. (a) Distribution of the deviation ε_{ex} for different η across various cases. (b) Sensitivity of varying φ across 90° (solid lines) versus 60° (dashed lines) junction angle cases.

Relative to the continuity-based simplified methodology, this study achieves significantly enhanced precision in $u_{\max}$ estimation (2.88% vs. 21.2% mean relative error). The simplified methodology derives the width of the vena contracta through Equation B5, subsequently computing cross-sectional average longitudinal velocity via mass conservation. Systematic comparisons in Tables D1 and D2 juxtapose predictions from both methodologies against numerical simulations, quantifying relative errors between each computational and simulated value.

The selection between single or dual control volume models for calculating $u_{\max}$ depends on the mixing mode of the shear layer at the widest cross-section of the recirculation zone. This determination can be made using either the theoretical model proposed by Sukhodolov et al. (2023) for describing shear layer mixing processes or through mixed dye visualization experiments (Sukhodolov & Rhoads, 2001).

7.1. Sensitive Analyses of Empirical Correction Factor φ

Shabayek et al. (2002) employed the two-control volume method to calculate the water depths upstream and downstream of the main and tributary channels, but their selection of the control volume interface did not account for the effects of θ and secondary flows. In the proposed models, the calculation of the average flow velocity within the control volume depends on the position of the hypothetical interface. Therefore, the ability to accurately predict $u_{\max}$ relies on the accurate determination of the hypothetical interface position. However, predicting the extent of shear layer distortion caused by secondary flows in the CHZ is challenging (Rhoads & Sukhodolov, 2008), which makes it difficult to accurately predict the hypothetical interface position. This study introduces φ in Equation 15 to represent the influence of secondary flows on the position of the hypothetical interface. Figure 18a illustrates the discrepancy between the hypothetical interface positions at the cross-section of the maximum flow velocity calculated without the empirical correction factor φ, namely $\varphi = 0$, and those obtained from numerical simulations. The deviation ε_{ex} is defined as:

$$\varepsilon_{\text{ex}} = |W_{1,\text{calculated}} - W_{1,\text{simulated}}| \quad (32)$$

Figure 18a depicts ε_{ex} variations without discernible trends. These values correlate with secondary flow intensity in the confluence zone, which scales with θ and η but decays longitudinally (Pein et al., 2018; Shen et al., 2022; Yuan, Zhu, et al., 2022). The interplay between θ, η, and downstream development distance governs the observed trendless distribution. Sensitive analyses of φ for the wake mode are conducted, as shown in Figure 18b. The value of φ varies from 0 to 0.03, whereas other parameters remain constant. Figure 18b indicates that the impact of φ variations on the computed results is not uniform. For cases in which $u_{\max}$ occurs in V_2 (e.g., cases A2, A5, B2, B4), variations in φ have a significantly greater effect on the computed results. This is because φ governs the calculation of W_2, and the effective width of V_2 exceeds that of V_1; accordingly, φ variations are more pronounced in subsequent computations in V_2, as reflected in u_2 (Equation 17). As φ increases, u_1 increases while u_2 decreases, resulting in a larger u/u_d; however, the trends in u/u_d changes vary, owing to the additional influence of the boundary conditions. The empirical coefficient $\varphi = 0.02$ adopted in this study was determined through error minimization protocols.

7.2. Limitations of the Present Study and Future Developments

This study introduces the hypothetical roughness coefficients for the recirculation zone boundary and the hypothetical interface, extending the method used for calculating velocity distribution in asymmetric channels to determine $u_{\max}$. However, this approach also presents certain drawbacks. There is a subtle deviation between the actual position of $u_{\max}$ and the zero shear stress plane, which depends on the roughness difference between the two boundaries of the control volume (Parthasarathy & Muste, 1994).

The expression for the coefficient ζ was derived specifically for two junction angles, limiting its broader practical applicability. However, in confluences with smaller θ (e.g., 30°), the maximum velocity phenomenon is less pronounced. This occurs because at smaller junction angles, the recirculation zone becomes significantly narrower or may not form, thereby suppressing the development of the maximum velocity that would otherwise arise from the reduction in the effective flow cross-section.

The mathematical model proposed in this study has been validated exclusively against data sets obtained from flume experiments. Its formulation is based on idealized laboratory conditions, incorporating sharp junction angles and rectangular cross-sections—features that diverge significantly from natural confluences, which often feature smoothly curved junction angles (Biron et al., 1993; Roy et al., 1988), channel discordance (Li et al., 2022), and velocity dip due to secondary flows (Yuan et al., 2024). Smooth junction angles may limit the applicability of the proposed equation for predicting recirculation zone width. Furthermore, the model does not account for factors such as channel discordance or velocity dip induced by secondary currents.

8. Conclusion

To investigate the hydrodynamic characteristics within the confluence channel, the factors influencing the maximum longitudinal flow velocity were studied. Utilizing the control volume method and mixing length theory, an analytical model for calculating the maximum longitudinal flow velocity at a confluence was developed. The accuracy of the proposed model was validated using the results from a numerical simulation.

1. Proposed a new interface position at the location of the minimum flow velocity within the shear layer. This interface position takes into account the effects of the junction angle, discharge ratio, and secondary flow.
2. We characterized the maximum flow velocity in the confluence channel by the maximum flow velocity at the section where the width of the recirculation zone is greatest, simplifying the solution process. Relative error analysis confirms a mean deviation of 1.6% between approximated and simulated maximum velocities, demonstrating the validity of this modeling methodology.
3. Considering the effects of the shear layer being in two modes on the flow velocity, we applied the double-layer assumption, typically used for velocity distribution in asymmetric channels, for the calculation of the maximum flow velocity.

Although this study presents a mathematical model that can effectively calculate the maximum longitudinal flow velocity, there are still aspects that can be improved in future work. For instance, quantitatively analyzing the impact of secondary flows on the longitudinal velocity distribution and determining the range of the empirical coefficient φ through further experimental studies or numerical simulations.

Appendix A: Grid Sensitivity Analysis

Grid sensitivity analysis focused on the downstream confluence velocity field critical for defining recirculation zones. The medium mesh (5.7M cells, $2 \times 10 \times 10$ mm) achieved 2 mm resolution at critical junction interfaces. Fine mesh (9.2M cells, $0.8 \times 10 \times 10$ mm) and coarse mesh (2.6M cells, $4 \times 10 \times 10$ mm) configurations were comparatively evaluated. Velocity profiles along horizontal longitudinal transects ($y = 0.5$ m, $z = 0.06$ m) were

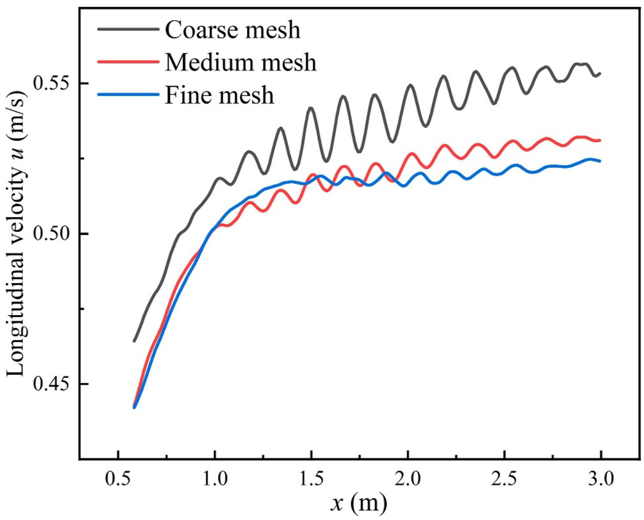

Figure A1. Longitudinal velocity profiles were computed using three distinct grid configurations.

analyzed across all three mesh configurations. Figure A1 presents the computational results of the three grids. Although differences between the medium and fine grids peaked at approximately 2%, the absolute deviation remained below 0.011 m/s, well below the deviations observed between experimental and simulated results; further grid refinement has minimal impact on the computational results. When the minimum grid cell size is 0.02 m, the Grid Convergence Index value is 1.67% (Celik et al., 2008), which is below 3%, meeting the computational accuracy requirements.

Appendix B: Calculation of the Maximum Width of the Recirculation Zone

The factors influencing the maximum width of the recirculation zone, namely θ and η, have been demonstrated by experimental measurements, numerical simulations, and analytical formulas (Best & Reid, 1984; Shen et al., 2022). In the mathematical models, the computational domain comprises grid cells near the free surface within the confluence region; each grid cell has a constant water depth Δh, with its top layer connected to the free surface and sharing the same cross-sectional area as the confluence channel. Because Δh is very small, a uniform velocity distribution is assumed in the inlet and outlet sections of each control volume. Using this modeling approach, the depth-averaged maximum width of the recirculation zone at the free surface height (FBS) is computed within the computational domain, representing the maximum width of the recirculation zone at the free surface. The shear layer is characterized by quasi-two-dimensional vortex structures, meaning that the large-scale turbulence generated by transverse shear is two-dimensional (Sukhodolov & Rhoads, 2001). Therefore, the above modeling approach is reasonable. The derivation was conducted exclusively within the surface computational grid, and the result of the model outputs characterized free-surface profiles.

A rectangular coordinate system is established as shown in Figure B1, with the midpoint of the tributary downstream section (TDS) as the origin and the straight line along the TDS as the n-axis. At the cross-section with the maximum width of the recirculation zone, it is conventionally assumed that the effective width of the control volume is formed by the boundary of the recirculation zone and the opposing wall (MCS). It is possible to derive a relationship between the width of the effective flow cross-section and the average flow velocity based on the principle of mass conservation. Notably, at the MCS cross-section, the direction of the boundary tangent aligns with the opposing wall, and the conservation of mass within the FBS is expressed as:

$$Q_{\text{MCS}} = \Delta h_{\text{MCS}} W_{\text{MCS}} u_{\text{MCS}} = \mu W_d \Delta h_{\text{MCS}} u_{\text{MCS}} \tag{B1}$$

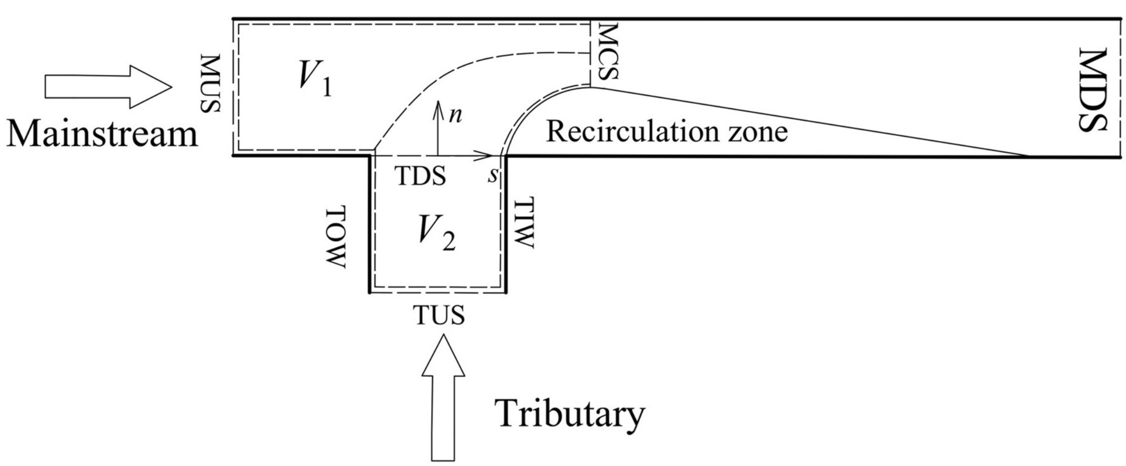

Figure B1. Schematic diagram of the n-axis and s-axis Cartesian coordinate system and naming convention for cross-sections and walls.

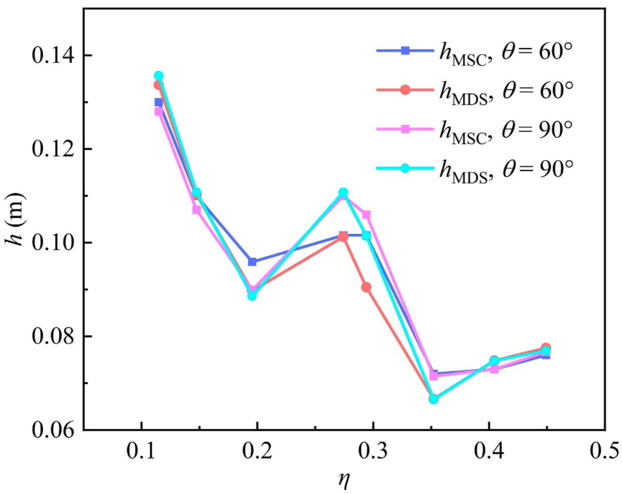

Figure B2. Comparison of water depths on the MDS and MCS cross-sections.

where Q_{MCS} is the discharge through the MCS cross-section in the FBS; μ is the maximum flow contraction coefficient given by $\mu = W_{\mathrm{MCS}}/W_d$; u_{MCS} is the average cross-sectional flow velocity along the direction of s-axis at the MCS cross-section; and Δh is the grid height for water surface elevation calculation grid. The relationship between μ, θ, and η can be determined by establishing the energy and momentum equations for the control volume composed of the MCS, TUS, and MUS cross-sections within the FBS. The energy conservation equation for the control volume is represented by:

$$\left(\Delta h_{\mathrm{TUS}} + \frac{\alpha_{\mathrm{TUS}} Q_{\mathrm{TUS}}^2}{2gA_{\mathrm{TUS}}^2}\right) Q_{\mathrm{TUS}} + \left(\Delta h_{\mathrm{MUS}} + \frac{\alpha_{\mathrm{MUS}} Q_{\mathrm{MUS}}^2}{2gA_{\mathrm{MUS}}^2}\right) Q_{\mathrm{MUS}} = \left(\Delta h_{\mathrm{MCS}} + \frac{\alpha_{\mathrm{MCS}} Q_{\mathrm{MCS}}^2}{2gA_{\mathrm{MCS}}^2}\right) Q_{\mathrm{MCS}} \tag{B2}$$

where A is the effective cross-sectional area of the channel given by $A = \Delta hW$; assuming the upstream water depths are equal (Creelle et al., 2016; Hager, 1987), namely $\Delta h_{\mathrm{TUS}} = \Delta h_{\mathrm{MUS}}$; Q is the discharge through the effective cross-section within the FBS; α is the energy correction coefficient. The momentum equation in the direction of the control volume neglects bed shear stresses, constituted by the MCS, TUS, and MUS sections at the water surface, is articulated as:

$$\frac{\beta_{\mathrm{TUS}} Q_{\mathrm{TUS}}^2}{g\Delta h_{\mathrm{TUS}} W_{\mathrm{TUS}}}\cos(\theta) + \frac{1}{2}\Delta h_{\mathrm{TUS}}^2 W_{\mathrm{TUS}}\cos(\theta) + \frac{1}{2}\Delta h_{\mathrm{MUS}}^2 W_{\mathrm{MUS}} + \frac{\beta_{\mathrm{MUS}} Q_{\mathrm{MUS}}^2}{g\Delta h_{\mathrm{MUS}} W_{\mathrm{MUS}}} = \frac{\beta_{\mathrm{MCS}} Q_{\mathrm{MCS}}^2}{g\Delta h_{\mathrm{MCS}} W_{\mathrm{MCS}}} + \frac{1}{2}\Delta h_{\mathrm{MCS}}^2 W_{\mathrm{MCS}} + \frac{P^*}{\rho g}\Delta h_{\mathrm{TUS}} W_{\mathrm{TUS}}\sin(\theta) \tag{B3}$$

where β is the momentum correction coefficient; P^* is the average hydrodynamic pressure exerted on the side walls of the tributary channel, calculated as P_{TIW}-P_{TOW}, where P is the hydrostatic pressure. Hager (1987) posited that P^* solely correlates with the pressures at the TUS and MCS sections, thereby P^* can be articulated as:

$$P^* = \frac{P_{\mathrm{TUS}} + \zeta P_{\mathrm{MCS}}}{1+\zeta} = \frac{1}{2}\rho g \frac{\Delta h_{\mathrm{TUS}} + \zeta \Delta h_{\mathrm{MCS}}}{1+\zeta} \tag{B4}$$

where ζ is a dimensionless parameter. Upon synthesizing Equations B2 through B3, one can ascertain the relationship among μ, η and θ. The maximum flow contraction coefficient is delineated as:

$$\mu = \frac{\alpha_{\mathrm{MCS}}\left(1 + Y + \frac{\zeta\sin(\theta)}{1+\zeta}\overline{W}Y\right)}{2\beta_{\mathrm{MCS}} + \sqrt{4\beta_{\mathrm{MCS}}^2 - \alpha_{\mathrm{MCS}}\left[1 + \frac{1}{Y} + \frac{\zeta\sin(\theta)}{1+\zeta}\overline{W}\right]\left\{4\beta_{\mathrm{MUS}}(1-\eta)^2 + 4\beta_{\mathrm{TUS}}\eta^2\cos(\theta)/\overline{W} - \left[1 + \frac{1}{Y} + \overline{W}\frac{\zeta\sin(\theta)}{1+\zeta}\right]\left[\alpha_{\mathrm{MUS}}(1-\eta)^3 + \alpha_{\mathrm{TUS}}\eta^3/\overline{W}^2\right]\right\}}} \tag{B5}$$

where $\overline{W}$ is the width ratio, defined as $\overline{W} = W_{\mathrm{TUS}}/W_{\mathrm{MUS}}$, Y is the depth ratio, defined as $Y = \Delta h_{\mathrm{MUS}}/\Delta h_{\mathrm{MCS}}$. The estimation of Δh_{MUS} in FBS employs a simplified approach. Figure B2 illustrates the relationship between h_{MCS} and h_{MDS} under selected flow conditions, revealing statistically comparable ratios.

We therefore postulate $\Delta h_{\mathrm{MCS}}/\Delta h_{\mathrm{MUS}} = h_{\mathrm{MUS}}/h_{\mathrm{MDS}} = h_{\mathrm{MUS}}/h_{\mathrm{MCS}}$ based on this equivalence (Creelle et al., 2016). The computation of $h_{\mathrm{MUS}}/h_{\mathrm{MDS}}$ follows the one-dimensional model developed by Shabayek et al. (2002), implementing a two-control volume approach that partitions post-confluence flows into mainstream and tribute domains. Given the assumption of equal upstream water depths in both channels, the momentum equation for the mainstream control volume alone suffices to determine $h_{\mathrm{MCS}}/h_{\mathrm{MDS}}$, defined as:

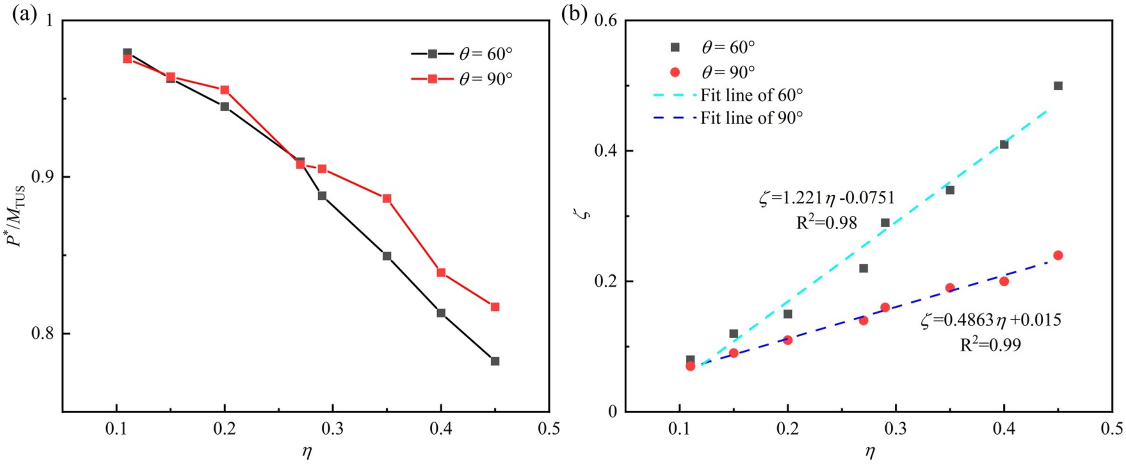

Figure B3. (a) The average hydrodynamic pressure from the tributary. (b) Variation of ζ with discharge ratio.

$$-\rho Q_{\text{MUS}}u_{\text{MUS}} + \rho Q_{\text{MUS}}u_{\text{MDS}} = \frac{1}{2}\rho g W_{\text{MUS}}h_{\text{MDS}}^2 - \frac{1}{2}\rho g W_{\text{MUS}}h_{\text{MDS}}^2(1-\eta) + \frac{\rho g}{2}h_{\text{MUS}}^2[W_{\text{MUS}}(1-\eta) - W_{\text{MUS}}]$$
$$+\rho g\left[\frac{A_{\text{MUS}} + A_{\text{MDS}}(1-\eta)}{2}\right]LS_0 - 2K^*\rho\left(u_{\text{MUS}}^2 - u_{\text{TUS}}^2\right)h_{\text{MUS}}[2W_{\text{MUS}}\eta(1-\eta)]$$
$$-\rho\left(\frac{u_{\text{MDS}}}{C^*}\right)^2 L[W_{\text{MUS}}(1-\eta) + h_{\text{MDS}}] \tag{B6}$$

where L is the outer length of the mainstream control volumes; K^* is the coefficient of hypothetical interfacial shear, defined as $K^* = 0.0092\theta - 0.1855$; C^* is the nondimensional Chey coefficient, and the value is 17.

Currently, Equations B5 and B6 form a nonlinear equation system with an equivalent count of equations and unknowns. The nonlinear system has a unique solution, and the least squares method yields approximate values for both μ at the water surface position, corresponding to the effective cross-sectional width of the flow within the contraction section. At larger θ, the tributary flow exhibits pre-merging deflection, leading to a merging angle smaller than the geometric junction angle. This deflection magnitude increases proportionally with θ (Hager, 1989), while the empirical coefficient ζ in Equation B4 mitigates discrepancies arising from this phenomenon. Alternatively, employing the technique of dye tracer injection proximal to the water surface at the downstream corner (Hsu, Wu, & Lee, 1998; Webber & Greated, 1966) facilitates the ascertainment of the maximum width of the recirculation zone at the water surface position.

The energy coefficient α (Equation B2) and momentum coefficient β (Equation B3) depend on θ, η, and the geometry of the downstream channel (Hsu, Wu, & Lee, 1998, Hsu, Lee, & Chang, 1998; Ramamurthy et al., 1988). These coefficients peak at the maximum recirculation zone width, increasing initially and then decreasing along the flow path (Luo et al., 2018). Currently, there is no unified theoretical equation for determining α and β (Li et al., 2022). In this study, α and β are derived following the formulation in Hsu, Wu, and Lee (1998). In this study, α and β are derived following the formulation in Hsu, Wu, and Lee (1998). However, since Hsu, Wu, and Lee (1998) only provide empirical formulas for the condition of a 90° confluence with equal channel widths, this study adopts the average values calculated from 20 scenarios based on the empirical formulas to reduce the deviation between the actual and calculated α and β, defined as:

$$\alpha = \frac{1}{20}\sum_{i=1}^{20}\left(1 + \frac{0.06}{\eta_i}\right)$$
$$\beta = \frac{1}{20}\sum_{i=1}^{20}\left(1 + \frac{0.03}{\eta_i}\right) \tag{B7}$$

The dimensionless parameter ζ, governing P^* depends on η and θ. Figure B3a plots dimensionless P^*/M_{TUS} against η and θ (where M_{TUS} denotes the mean momentum flux at section TUS). P^*/M_{TUS} decreases as η increases progressively and is generally larger at a junction angle of 90° than at 60°. This trend arises because increasing η or decreasing θ reduces the deflection of tributary flow (Creelle et al., 2016; Hager, 1989), thereby decreasing the water depth differential across its sidewalls, leading to a reduction in P^*. The value of ζ was systematically quantified across all cases as shown in Figure B3b, revealing an approximately linear correlation with η at fixed θ. The empirical expression derived from the fitting procedure is formulated as:

$$\begin{cases} \zeta = 1.221\eta - 0.0751 & \theta = 60\,° \\ \zeta = 0.486\eta + 0.015 & \theta = 90\,° \end{cases} \tag{B8}$$

Appendix C: Dimensionless Friction Coefficients

The Darcy-Weisbach friction coefficient for the wall is derived by combining the Chezy formula with the Manning equation. The friction coefficient for the wall can be expressed as:

$$f_b = \frac{8gn_b^2}{R_b^{1/3}} \tag{C1}$$

where n_b is the Manning's roughness coefficient of the wall, and R_b is the hydraulic radius of the wall shear stress layer. For asymmetric channels, such as ice-covered channels, R_b can be determined by relating the roughness coefficients of the shear walls on both sides of the control volume to the hydraulic radius of the flow cross-section (Wang et al., 2020). However, in channel confluences, the hypothetical interface and the boundary of the recirculation zone lack a defined roughness coefficient. To compute R_b, we assume the presence of hypothetical roughness coefficients on the hypothetical interface and the boundary of the recirculation zone, equivalent to the n_b. By utilizing the hypothetical interface roughness coefficient, the relationship between R_b and the hydraulic radius R_{V_i} of the flow cross-section within control volumes was derived. From Equation C1, the relationships between the shear coefficients and the hypothetical roughness coefficients at the hypothetical interface and the boundary of the recirculation zone are given as:

$$\begin{aligned} f_{\text{sh}} &= \frac{8gn_{\text{sh}}^2}{R_{\text{sh}}^{1/3}} \\ f_{\text{re}} &= \frac{8gn_{\text{re}}^2}{R_{\text{re}}^{1/3}} \end{aligned} \tag{C2}$$

where n_{sh} and n_{re} are the hypothetical roughness coefficients at the hypothetical interface and the boundary of the recirculation zone, respectively; R_{sh} and R_{re} are the hydraulic radiuses of the hypothetical interface shear stress layer and the recirculation zone shear stress layer, respectively. Using the Chezy formula and the Manning equation, the expressions for the depth-averaged streamwise velocities in the recirculation zone shear stress layer, the wall shear stress layer, and the hypothetical interface shear stress layer are derived as:

$$\begin{aligned} \overline{u}_b &= \frac{R_b^{2/3} J_b^{1/2}}{n_b} \\ \overline{u}_{re} &= \frac{R_{\text{re}}^{2/3} J_{\text{re}}^{1/2}}{n_{re}} \\ \overline{u}_{\text{sh}} &= \frac{R_{\text{sh}}^{2/3} J_{\text{sh}}^{1/2}}{n_{\text{sh}}} \end{aligned} \tag{C3}$$

where J is the hydraulic slope of each shear stress layer; $\overline{u}$ is the average flow velocity in each shear stress layer. Utilizing the common assumptions in asymmetric channels (Ervine et al., 2000), specifically within V_1,

$\overline{u}_b = \overline{u}_{\mathrm{sh},V_1}$, $J_b = J_{\mathrm{sh},V_1}$ and within V_2, $\overline{u}_{\mathrm{re}} = \overline{u}_{\mathrm{sh},V_2}$, $J_{\mathrm{re}} = J_{\mathrm{sh},V_2}$. Accordingly, combining Equation C3 the relationship between R_{b,V_1} and R_{sh,V_1}, as well as those between R_{re,V_2} and R_{sh,V_2} can be present as

$$\begin{aligned} \frac{R_{b,V_1}}{R_{\mathrm{sh},V_1}} &= \frac{n_b^{3/2}}{n_{\mathrm{sh}}^{3/2}} \\ \frac{R_{\mathrm{re},V_2}}{R_{\mathrm{sh},V_2}} &= \frac{n_{\mathrm{re},\,V_2}^{3/2}}{n_{\mathrm{sh}}^{3/2}} \end{aligned} \tag{C4}$$

The comprehensive hydraulic radius R_{V_1} within V_1 and the comprehensive hydraulic radius R_{V_2} within V_2 are represented as:

$$\begin{aligned} R_{V_1} &= \frac{A_b + A_{\mathrm{sh}}}{\chi_b + \chi_{\mathrm{sh}}} = \frac{(A_b/\chi_b)\chi_b/\chi_{\mathrm{sh}} + A_{\mathrm{sh}}/\chi_{\mathrm{sh}}}{1 + \chi_b/\chi_{\mathrm{sh}}} = \frac{i + n_{\mathrm{sh}}^{3/2}/n_b^{3/2}}{1+i} R_{b,V_1} \\ R_{V_2} &= \frac{A_{\mathrm{re},V_2} + A_{\mathrm{sh}}}{\chi_{\mathrm{re},V_2} + \chi_{\mathrm{sh}}} = \frac{(A_{\mathrm{re},V_2}/\chi_{\mathrm{re},V_2})\chi_{\mathrm{re},V_2}/\chi_{\mathrm{sh}} + A_{\mathrm{sh}}/\chi_{\mathrm{sh}}}{1 + \chi_{\mathrm{re},V_2}/\chi_{\mathrm{sh}}} = \frac{i + n_{\mathrm{sh}}^{3/2}/n_{\mathrm{re},V_2}^{3/2}}{1+i} R_{\mathrm{re},V_2} \end{aligned} \tag{C5}$$

where χ_b, χ_{sh} and χ_{re,V_2} are respectively the dimensionless wetted perimeters of the wall per unit depth, the hypothetical interface per unit depth and the recirculation zone per unit depth. At the section MCS, χ_b and χ_{re,V_2} can be taken as χ_{sh}, namely $i = 1$. The comprehensive hydraulic radius within V_1 and V_2 are equal to half the width of the shear stress layer, that is, $R_{V_1} = W_1/2$, $R_{V_2} = W_2/2$, thus, the hydraulic radius of the wall shear stress layer and the hydraulic radius of the recirculation shear stress are defined as:

$$\begin{aligned} R_{b,V_1} &= \frac{W_1 n_b^{3/2}}{n_b^{3/2} + n_{\mathrm{sh}}^{3/2}} \\ R_{\mathrm{re},V_2} &= \frac{W_2 n_{\mathrm{re},V_2}^{3/2}}{n_{\mathrm{re},V_2}^{3/2} + n_{\mathrm{sh}}^{3/2}} \end{aligned} \tag{C6}$$

For V_3, following the same assumptions as in V_1 and V_2, the relationship between R_{b,V_3} and R_{re,V_3} is derived as:

$$\frac{R_{b,V_3}}{R_{\mathrm{re},V_3}} = \frac{n_b^{3/2}}{n_{\mathrm{re},V_3}^{3/2}} \tag{C7}$$

The comprehensive hydraulic radius R_{V_3} within V_3 is derived as:

$$R_{V_3} = \frac{A_b + A_{re}}{\chi_b + \chi_{re}} = \frac{1 + n_b^{3/2}/n_{re,V_3}^{3/2}}{2} R_{re,V_3} \tag{C8}$$

The comprehensive hydraulic radius R_{V_3} is equal to half the width of the flow cross-section, that is, $R_{V_3} = W_3/2$. Thus, R_{re,V_3} is expressed as

$$R_{\mathrm{re},V_3} = \frac{W_3 n_{\mathrm{re},V_3}^{3/2}}{n_b^{3/2} + n_{\mathrm{re},V_3}^{3/2}} \tag{C9}$$

Thus, the expressions for the friction coefficient are as follows:

10.1029/2025WR041424

$$
\begin{aligned}
f_b &= \frac{8gn_b^2}{\left(\frac{W_1 n_b^{3/2}}{n_b^{3/2}+n_{\mathrm{sh}}^{3/2}}\right)^{1/3}} \\
f_{\mathrm{re},V_2} &= \frac{8gn_{\mathrm{re},V_2}^2}{\left(\frac{W_2 n_b^{3/2}}{n_{\mathrm{re},V_2}^{3/2}+n_{\mathrm{sh}}^{3/2}}\right)^{1/3}} \\
f_{re,V_3} &= \frac{8gn_{\mathrm{re},V_3}^2}{\left(\frac{W_3 n_{\mathrm{re},V_3}^{3/2}}{n_b^{3/2}+n_{\mathrm{re},V_3}^{3/2}}\right)^{1/3}}
\end{aligned}
\tag{C10}
$$

Appendix D: Relative Errors Between Each Computational and Simulated Value

This appendix section discusses the calculation of the maximum flow velocity using the mass conservation method. The expressions for the maximum velocity in each control volume are given below:

$$u_{\max\ 1,V_1} = \frac{Q_{\mathrm{MUS}}}{W_1 H} \tag{D1}$$

$$u_{\max\ 1,V_2} = \frac{Q_{\mathrm{TUS}}}{W_2 H} \tag{D2}$$

$$u_{\max\ 1,V_3} = \frac{Q_{\mathrm{MUS}} + Q_{\mathrm{TUS}}}{W_3 H} \tag{D3}$$

where $u_{\max\ 1,V_i}$ represents the longitudinal depth-averaged maximum velocity in each control volume calculated by the simplified method; W_i denotes the effective flow area in each control volume, which is determined using the same approach as in this study (Equations B5 and 15). Tables D1 and D2 systematically compare the

Table D1
Case at a 60° Junction Angle

Case	A1	A2	A3	A4	A5	A6	A7	A8	A9	A10
$u_{\max}$ (m/s)	0.685	0.641	0.574	0.736	0.697	0.607	0.668	0.715	0.599	0.644
$u_{\max1}$ (m/s)	0.544	0.503	0.446	0.565	0.523	0.461	0.503	0.536	0.459	0.495
ε_{r1} (%)	20.5	21.6	22.4	23.2	24.9	24.1	24.7	25	23.3	23.1
$u_{\max2}$ (m/s)	0.674	0.619	0.598	0.713	0.696	0.599	0.651	0.717	0.598	0.635
ε_{r2} (%)	1.55	3.3	4.14	3.11	0.12	1.26	2.67	0.29	0.05	1.35

Table D2
Case at a 90° Junction Angle

Case	B1	B2	B3	B4	B5	B6	B7	B8	B9	B10
$u_{\max}$ (m/s)	0.726	0.691	0.642	0.716	0.690	0.644	0.703	0.747	0.625	0.653
$u_{\max1}$ (m/s)	0.574	0.538	0.499	0.582	0.564	0.525	0.581	0.623	0.512	0.534
ε_{r1} (%)	20.9	22.1	22.3	18.7	18.3	18.5	17.4	16.6	18.1	18.2
$u_{\max2}$ (m/s)	0.718	0.671	0.622	0.755	0.651	0.664	0.685	0.722	0.592	0.605
ε_{r2} (%)	1.07	2.87	3.12	5.44	5.7	3.16	2.49	3.36	5.3	7.26

Note. $u_{\max}$ is the maximum flow velocity derived from the simulation, $u_{\max1}$ and ε_{r1} are respectively the maximum flow velocity calculated with the model described above and the relative error between $u_{\max}$ and $u_{\max1}$. $u_{\max2}$ and ε_{r1} are respectively the maximum flow velocity calculated with the model proposed in the manuscript and the relative error between $u_{\max}$ and $u_{\max2}$.

simplified method, the calculation method proposed in this paper, and numerical prediction results, along with the relative errors between both calculated results and the true values.

Nomenclature

The following symbols are used in this paper:

η	Discharge ratio (−)
Q	Discharge (m^3/s)
W	Cross-sectional width (m)
W_d	Main channel width (m)
H	Water depth (m)
W_1, W_2, W_3	Width of control volume V_1, V_2, V_3 (m)
Δh	Flow depth of flow blocks (m)
s, x	Streamwise directions (−)
S_0	Channel bed slope (−)
ρ	Fluid density (kg/m^3)
g	Gravitational acceleration (m/s^2)
n, y	Lateral directions (−)
u_{max}	Maximum temporal average velocity components in x directions (m/s)
$u_{max,re}$	Maximum velocity at the cross-section MCS (m/s)
u, v	Temporal average velocities in streamwise, lateral directions (m/s)
p	Pressure force (N)
θ	Angle between the main and tributary channels (°)
μ	Maximum flow contraction coefficient (−)
A	Effective cross-sectional area (m^2)
α	Energy correction coefficient (−)
β	Momentum correction coefficient (−)
P^*	Average hydrodynamic pressure exerted on the side walls of the tributary channel (N)
ζ, φ	Empirical coefficients in Equations 18 and 21 (−)
f	Shear coefficient (−)
τ	Shear stress (N/m^2)
n	Manning roughness coefficient (−)
R	Hydraulic radius (m)
J	Hydraulic slope (−)
l	Mixing length (m)
κ	Karman constant (−)
y'	Position of maximum flow velocity (m)

χ	Dimensionless wetted perimeter per unit width (−)
C_1, C_2, C_3	Integration constants in Equations 25, 26 and 31 (−)

The following subscripts are used in this paper:

t, *m*	Abbreviations of the tributary and main channel
V_1, V_2, V_3	Abbreviations of control volume
re, *sh, b*	Abbreviations of the recirculation zone, interface, and wall shear stress layer

Conflict of Interest

The authors declare no conflicts of interest relevant to this study.

Data Availability Statement

The software version used in this paper is OpenFOAM-10, which is available for download at the link: https://openfoam.org/download/10-macos/ (Greenshields, 2022). All the data used in this study are available through https://doi.org/10.5281/zenodo.15107248 (Feng et al., 2025).

Acknowledgments

This work was supported by the (Open Research Fund of MWR Key Laboratory of Lower Yellow River Channel and Estuary Regulation; Grant LYRCER202202), the (Yellow River Laboratory (Zhengzhou University) first-class project special fund project) (Grant YRL221R11 and YRL22YL03), the (Special Scientific Research Project of Yellow River Water Resources Protection Institute; Grant KYY-KYZX-2022-01), the (Natural Science Foundation of Henan; Grant 252300421946).

References

Ashmore, P. E. (1982). Laboratory modeling of gravel braided-stream morphology. *Earth Surface Processes and Landforms*, *7*(3), 201–225. https://doi.org/10.1002/esp.3290070301

Ashmore, P. E., Ferguson, R. I., Prestegaard, K. L., Ashworth, P. J., & Paola, C. (1992). Secondary flow in anabranch confluences of a braided, gravel-bed stream. *Earth Surface Processes and Landforms*, *17*(3), 299–311. https://doi.org/10.1002/esp.3290170308

Bennett, N. D., Croke, B. F. W., Guariso, G., Guillaume, J. H. A., Hamilton, S. H., Jakeman, A. J., et al. (2013). Characterising performance of environmental models. *Environmental Modelling & Software*, *40*, 1–20. https://doi.org/10.1016/j.envsoft.2012.09.011

Best, J. L. (1987). Flow dynamics at river channel confluences: Implications for sediment transport and bed morphology. In F. G. Ethridge, R. M. Flores, & M. D. Harvey (Eds.), *Recent developments in fluvial sedimentology* (Vol. 39, pp. 27–35). https://doi.org/10.2110/pec.87.39.0027

Best, J. L. (1988). Sediment transport and bed morphology at river channel confluences. *Sedimentology*, *35*(3), 481–498. https://doi.org/10.1111/j.1365-3091.1988.tb00999.x

Best, J. L., & Reid, I. (1984). Separation zone at open-channel junctions. *Journal of Hydraulic Engineering*, *110*(11), 1588–1594. https://doi.org/10.1061/(ASCE)0733-9429(1984)110:11(1588)

Biron, P., Roy, A., Best, J. L., & Boyer, C. J. (1993). Bed morphology and sedimentology at the confluence of unequal depth channels. *Geomorphology*, *8*(2–3), 115–129. https://doi.org/10.1016/0169-555X(93)90032-W

Boyer, C., Roy, A. G., & Best, J. L. (2006). Dynamics of a river channel confluence with discordant beds: Flow turbulence, bed load sediment transport, and bed morphology. *Journal of Geophysical Research*, *111*(F4). https://doi.org/10.1029/2005JF000458

Bradbrook, K. F., Biron, P. M., Lane, S. N., Richards, K. S., & Roy, A. G. (1998). Investigation of controls on secondary circulation in a simple confluence geometry using a three-dimensional numerical model. *Hydrological Rrocesses*, *12*(8), 1371–1396. https://doi.org/10.1002/(SICI)1099-1085(19980630)12:8<1371::AID-HYP620>3.0.CO;2-C

Bradbrook, K. F., Lane, S. N., & Richards, K. S. (2000). Numerical simulation of three-dimensional, time-averaged flow structure at river channel confluences. *Water Resources Research*, *36*(9), 2731–2746. https://doi.org/10.1029/2000WR900011

Canelas, O. B., Ferreira, R. M. L., & Cardoso, A. H. (2022). Hydro-morphodynamics of an open-channel confluence with bed discordance at dynamic equilibrium. *Water Resources Research*, *58*(1), 18. https://doi.org/10.1029/2021WR029631

Celik, I. B., Ghia, U., Roache, P. J., & Freitas, C. J. (2008). Procedure for estimation and reporting of uncertainty due to discretization in CFD applications. *Journal of fluids Engineering-Transactions of the ASME*, *130*(7). https://doi.org/10.1115/1.2960953

Chen, X., Zhu, D. Z., & Steffler, P. M. (2017). Secondary currents induced mixing at channel confluences. *Canada Journal of Civil Engineering*, *44*(12), 1071–1083. https://doi.org/10.1139/cjce-2016-0228

Cheng, Z. Y., & Constantinescu, G. (2018). Stratification effects on flow hydrodynamics and mixing at a confluence with a highly discordant bed and a relatively low velocity ratio. *Water Resources Research*, *54*(7), 4537–4562. https://doi.org/10.1029/2017WR022292

Constantinescu, G., & Gualtieri, C. (2024). River confluences: A review of recent field and numerical studies. *Environmental Fluid Mechanics*, *24*(6), 1143–1191. https://doi.org/10.1007/s10652-024-10002-4

Constantinescu, G., Koken, M., & Zeng, J. (2011). The structure of turbulent flow in an open channel bend of strong curvature with deformed bed: Insight provided by detached eddy simulation. *Water Resources Research*, *47*(5). https://doi.org/10.1029/2010WR010114

Constantinescu, G., Miyawaki, S., Rhoads, B., Sukhodolov, A., & Kirkil, G. (2011b). Structure of turbulent flow at a river confluence with momentum and velocity ratios close to 1: Insight provided by an eddy-resolving numerical simulation. *Water Resources Research*, *47*(5), 16. https://doi.org/10.1029/2010WR010018

Creelle, S., Schindfessel, L., & De Mulder, T. (2016). Modelling of the tributary momentum contribution to predict confluence head losses. *Journal of Hydraulic Research*, *55*(2), 175–189. https://doi.org/10.1080/00221686.2016.1212941

Cuss, C. W., Ghotbizadeh, M., Grant-Weaver, I., Javed, M. B., Noernberg, T., & Shotyk, W. (2021). Delayed mixing of iron-laden tributaries in large boreal rivers: Implications for iron transport, water quality and monitoring. *Journal of Hydrology*, *597*, 12. https://doi.org/10.1016/j.jhydrol.2020.125747

Danen-Louwerse, H., Lijklema, L., & Coenraats, M. (1993). Iron content of sediment and phosphate adsorption properties. *Hydrobiologia*, *253*(1), 311–317. https://doi.org/10.1007/BF00050751

De Serres, B., Roy, A. G., Biron, P., & Best, J. L. (1999). Three-dimensional structure of flow at a confluence of river channels with discordant beds. *Geomorphology*, *26*(4), 313–335. https://doi.org/10.1016/S0169-555X(98)00064-6

Einstein, H. A. (1942). Formulas for the transportation of bed-load. *Transactions of ASCE*, *107*(2140), 561–597. https://doi.org/10.1061/taceat.0005468

Ervine, D. A., Babaeyan-Koopaei, K., & Sellin, R. H. J. (2000). Two-dimensional solution for straight and meandering overbank flows. *Journal of Hydraulic Engineering-ASCE*, *126*(9), 653–669. https://doi.org/10.1061/(ASCE)0733-9429(2000)126:9(653)

Feng, H., Li, Z., Gualtieri, C., Sun, B., Wang, F., & Li, K. (2025). Databet of "A semi-analytical model for predicting the maximum longitudinal flow velocity in the confluence channel" [Dataset]. *Zenodo*. https://doi.org/10.5281/zenodo.15107248

Fuentes-Pérez, J. F., Silva, A. T., Tuhtan, J. A., García-Vega, A., Carbonell-Baeza, R., Musall, M., & Kruusmaa, M. (2018). 3D modelling of non-uniform and turbulent flow in vertical slot fishways. *Environmental Modelling & Software*, *99*, 156–169. https://doi.org/10.1016/j.envsoft.2017.09.011

Ghostine, R., Mose, R., Vazquez, J., Ghenaim, A., & Grégoire, C. (2010). Two-dimensional simulation of subcritical flow at a combining junction: Luxury or necessity? *Journal of Hydraulic Engineering*, *136*(10), 799–805. https://doi.org/10.1061/(ASCE)HY.1943-7900.0000230

Greenshields, C. (2022). Openfoam user guide version 10 [Software]. *The OpenFOAM Foundation, Ltd*. https://doc.cfd.direct/openfoam/user-guide-v10/contents

Gualtieri, C., Abdi, R., Ianniruberto, M., Filizola, N., & Endreny, T. (2020). A 3D analysis of spatial habitat metrics about the confluence of Negro and Solimoes Rivers Brazil. *Ecohydrology*, *13*(1), e2166. https://doi.org/10.1002/eco.2166

Gualtieri, C., Ianniruberto, M., & Filizola, N. (2019). On the mixing of rivers with a difference in density: The case of the Negro/Solimões confluence, Brazil. *Journal of Hydrology*, *578*, 124029. https://doi.org/10.1016/j.jhydrol.2019.124029

Hager, W. H. (1987). Separation zone at open-channel junctions – Discussion. *Journal of Hydraulic Engineering-ASCE*, *113*(4), 539–543. https://doi.org/10.1061/(asce)0733-9429(1987)113:4(539)

Hager, W. H. (1989). Transitional flow in channel junctions. *Journal of Hydraulic Engineering-ASCE*, *115*(2), 243–259. https://doi.org/10.1061/(ASCE)0733-9429(1989)115:2(243)

Hsu, C. C., Lee, W. J., & Chang, C. H. (1998). Subcritical open-channel junction flow. *Journal of Hydraulic Engineering*, *124*(8), 847–855. https://doi.org/10.1061/(ASCE)0733-9429(1998)124:8(847)

Hsu, C. C., Wu, F. S., & Lee, W. J. (1998a). Flow at 90° equal-width open-channel junction. *Journal of Hydraulic Engineering-ASCE*, *124*(2), 186–191. https://doi.org/10.1061/(asce)0733-9429(1998)124:2(186)

Jiang, C., Constantinescu, G., Yuan, S., & Tang, H. (2023). Flow hydrodynamics, density contrast effects and mixing at the confluence between the Yangtze River and the Poyang Lake channel. *Environmental Fluid Mechanics*, *23*(2), 229–257. https://doi.org/10.1007/s10652-022-09848-3

Jin, T., Ramos, P. X., Mignot, E., Riviere, N., & De Mulder, T. (2023). On the delineation of the flow separation zone in open-channel confluences. *Advances in Water Resources*, *180*, 104525. https://doi.org/10.1016/j.advwatres.2023.104525

Kakavandi, H., Heidari, M. M., & Ghobadian, R. (2024). A numerical model for calculating velocity distribution in cross-section of an open channel. *Applied Water Science*, *14*(3), 11. https://doi.org/10.1007/s13201-023-02090-2

Kenworthy, S. T., & Rhoads, B. L. (1995). Hydrology control of spatial modes of suspended sediment concentration at a stream confluence. *Journal of Hydrology*, *168*(1–4), 251–263. https://doi.org/10.1016/0022-1694(94)02644-Q

Kim, J. S., Seo, I. W., Baek, D., & Kang, P. K. (2020). Recirculating flow-induced anomalous transport in meandering open-channel flows. *Advances in Water Resources*, *141*, 17. https://doi.org/10.1016/j.advwatres.2020.103603

Lane, S. N., Bradbrook, K. F., Richards, K. S., Biron, P. M., & Roy, A. G. (2000). Secondary circulation cells in river channel confluences: Measurement artefacts or coherent flow structures? *Hydrological Procseees*, *14*(11–12), 2047–2071. https://doi.org/10.1002/1099-1085(20000815/30)14:11/12<2047::AID-HYP54>3.0.CO;2-4

Lewis, Q., Rhoads, B., Sukhodolov, A., & Constantinescu, G. (2020). Advective lateral transport of streamwise momentum governs mixing at small river confluences. *Water Resources Research*, *56*(9), 20. https://doi.org/10.1029/2019WR026817

Lewis, Q. W., & Rhoads, B. L. (2015). Resolving two-dimensional flow structure in rivers using large-scale particle image velocimetry: An example from a stream confluence. *Water Resources Research*, *51*(10), 7977–7994. https://doi.org/10.1002/2015WR017783

Li, K., Tang, H. W., Yuan, S. Y., Xiao, Y., Xu, L., Huang, S. J., et al. (2022). A field study of near-junction-apex flow at a large river confluence and its response to the effects of floodplain flow. *Journal of Hydrology*, *610*, 19. https://doi.org/10.1016/j.jhydrol.2022.127983

Liu, X., Li, L., Hua, Z., Tu, Q., Yang, T., & Zhang, Y. (2019). Flow dynamics and contaminant transport in Y-shaped river channel confluences. *International Journal of Environmental Research and Public Health*, *16*(4), 572. https://doi.org/10.3390/ijerph16040572

Liu, X., Yu, L., Zhang, Y., Hua, Z., Li, X., Xue, H., & Chu, K. (2024). Release of perfluoroalkyl acids from sediments under the effects of the discharge ratio and flow flux at a Y-shaped confluence. *Water Research*, *260*, 121947. https://doi.org/10.1016/j.watres.2024.121947

Liu, X. D., Li, L. Q., Gu, L., Hua, Z. L., Zhang, Y., & Xue, H. Q. (2021). Distribution and release of perfluorinated compounds (PFCs) in water-sediment systems: The effect of confluence channels. *Science of the Total Environment*, *775*, 9. https://doi.org/10.1016/j.scitotenv.2021.145720

Lopez, P., Lluch, X., Vidal, M., & Morguí, J. A. (1996). Adsorption of phosphorus on sediments of the Balearic Islands (Spain) related to their composition. *Estuarine, Coastal and Shelf Science*, *42*(2), 185–196. https://doi.org/10.1006/ecss.1996.0014

Luo, H., Fytanidis, D. K., Schmidt, A. R., & García, M. H. (2018). Comparative 1D and 3D numerical investigation of open-channel junction flows and energy losses. *Advances in Water Resources*, *117*, 120–139. https://doi.org/10.1016/j.advwatres.2018.05.012

Lyubimova, T. P., Lepikhin, A. P., Parshakova, Y. N., Kolchanov, V. Y., Gualtieri, C., Roux, B., & Lane, S. N. (2020). A numerical study of the influence of channel-scale secondary circulation on mixing processes downstream of river junctions. *Water*, *12*(11), 24. https://doi.org/10.3390/w12112969

Mahmodinia, S., & Javan, M. (2021). Vortical structures, entrainment and mixing process in the lateral discharge of the gravity current. *Environmental Fluid Mechanics*, *21*(5), 1035–1067. https://doi.org/10.1007/s10652-021-09808-3

Miyawaki, S., Constantinescu, S. G., Kirkil, G., Rhoads, B., & Sukhodolov, A. (2009). Numerical investigation of three-dimensional flow structure at a river confluence. Paper presented at XXXIIIrd International Association Hydraulic Research Congress, Vancouver, B. C., Canada.

Miyawaki, S., Constantinescu, S. G., Rhoads, B., & Sukhodolov, A. (2010). On the three-dimensional flow structure at a river confluence with a high momentum ratio. Paper presented at International Conference on Fluvial Hydraulics, River Flow 2010, International Association for Hydro-Environment Engineering and Research, Braunschweig, Germany.

Parthasarathy, R. N., & Muste, M. (1994). Velocity measurements in asymmetric turbulent channel flows. *Journal of Hydraulic Engineering-ASCE*, *120*(9), 1000–1020. https://doi.org/10.1061/(ASCE)0733-9429(1994)120:9(1000)

Pein, J., Valle-Levinson, A., & Stanev, E. V. (2018). Secondary circulation asymmetry in a meandering, partially stratified estuary. *Journal of Geophysical Research: Oceans*, *123*(3), 1670–1683. https://doi.org/10.1002/2016JC012623

Ramamurthy, A. S., Carballada, L. B., & Tran, D. M. (1988). Combining open channel flow at right angled junctions. *Journal of Hydraulic Engineering*, *114*(12), 1449–1460. https://doi.org/10.1061/(ASCE)0733-9429(1988)114:12(1449)

Ramamurthy, A. S., Tran, D. M., & Carballada, L. B. (1994). Increased hydraulic resistance in combining open-channel flows. *Water Research*, *28*(6), 1505–1508. https://doi.org/10.1016/0043-1354(94)90319-0

Rhoads, B. L., & Johnson, K. K. (2018). Three-dimensional flow structure, morphodynamics, suspended sediment, and thermal mixing at an asymmetrical river confluence of a straight tributary and curving main channel. *Geomorphology*, *323*, 51–69. https://doi.org/10.1016/j.geomorph.2018.09.009

Rhoads, B. L., & Sukhodolov, A. N. (2001). Field investigation of three-dimensional flow structure at stream confluences: 1. Thermal mixing and time-averaged velocities. *Water Resources Research*, *37*(9), 2393–2410. https://doi.org/10.1029/2001WR000316

Rhoads, B. L., & Sukhodolov, A. N. (2004). Spatial and temporal structure of shear layer turbulence at a stream confluence. *Water Resources Research*, *40*(6), 13. https://doi.org/10.1029/2003WR002811

Rhoads, B. L., & Sukhodolov, A. N. (2008). Lateral momentum flux and the spatial evolution of flow within a confluence mixing interface. *Water Resources Research*, *44*(8). https://doi.org/10.1029/2007WR006634

Ribeiro, M. L., Blanckaert, K., Roy, A. G., & Schleiss, A. J. (2012). Hydromorphological implications of local tributary widening for river rehabilitation. *Water Resources Research*, *48*, 19. https://doi.org/10.1029/2011WR011296

Rice, S. P., Ferguson, R. I., & Hoey, T. B. (2006). Tributary control of physical heterogeneity and biological diversity at river confluences. *Canadian Journal of Fisheries and Aquatic Sciences*, *63*(11), 2553–2566. https://doi.org/10.1139/F06-145

Roy, A. G., Roy, R., & Bergeron, N. (1988). Hydraulic geometry and changes in flow velocity at a river confluence with coarse bed material. *Earth Surface Processes and Landforms*, *13*(7), 583–598. https://doi.org/10.1002/esp.3290130704

Schemel, L. E., Kimball, B. A., Runkel, R. L., & Cox, M. H. (2007). Formation of mixed Al-Fe colloidal sorbent and dissolved-colloidal partitioning of Cu and Zn in the Cement Creek-Animas River confluence, Silverton, Colorado. *Applied Geochemistry*, *22*(7), 1467–1484. https://doi.org/10.1016/j.apgeochem.2007.02.010

Schindfessel, L., Creëlle, S., & De Mulder, T. (2015). Flow modes in an open channel confluence with increasingly dominant tributary inflow. *Water*, *7*(9), 4724–4751. https://doi.org/10.3390/w7094724

Schindfessel, L., Creëlle, S., & De Mulder, T. (2017). How different cross-sectional shapes influence the separation zone of an open-channel confluence. *Journal of Hydraulic Engineering*, *143*(9), 12. https://doi.org/10.1061/(ASCE)HY.1943-7900.0001336

Shabayek, S., Steffler, P., & Hicks, F. (2002). Dynamic model for subcritical combining flows in channel junctions. *Journal of Hydraulic Engineering-ASCE*, *128*(9), 821–828. https://doi.org/10.1061/(ASCE)0733-9429(2002)128:9(821)

Shaheed, R., Mohammadian, A., & Gildeh, H. K. (2019). A comparison of standard k-ε and realizable k-ε turbulence models in curved and confluent channels. *Environmental Fluid Mechanics*, *19*(2), 543–568. https://doi.org/10.1007/s10652-018-9637-1

Shakibainia, A., Tabatabai, M. R. M., & Zarrati, A. R. (2010). Three-dimensional numerical study of flow structure in channel confluences. *Canadian Journal of Civil Engineering*, *37*(5), 772–781. https://doi.org/10.1139/L10-016

Shen, X., Gao, W. X., Cao, L. W., Li, S., Cai, H. J., Li, R., & Hodges, B. R. (2023). Characteristics of water free-surface with different momentum ratio at 45° confluence. *Journal of Hydrology*, *623*, 129787. https://doi.org/10.1016/j.jhydrol.2023.129787

Shen, X., Hodges, B. R., Li, R., Li, Z., Fan, J. L., Cui, N. B., & Cai, H. J. (2021). Factors influencing distribution characteristics of total dissolved gas supersaturation at confluences. *Water Resources Research*, *57*(6), 25. https://doi.org/10.1029/2020WR028760

Shen, X., Li, R., Cai, H., Feng, J., & Wan, H. (2022). Characteristics of secondary flow and separation zone with different junction angle and flow ratio at river confluences. *Journal of Hydrology*, *614*, 128537. https://doi.org/10.1016/j.jhydrol.2022.128537

Shen, X., Li, R., Hodges, B. R., Feng, J. J., Cai, H. J., & Ma, X. Y. (2019). Experiment and simulation of supersaturated total dissolved gas dissipation: Focus on the effect of confluence types. *Water Research*, *155*, 320–332. https://doi.org/10.1016/j.watres.2019.02.056

Shi, X., Jin, Q., Chen, H., Tao, H., & Song, T. (2025). Analysis of pollutant diffusion characteristics with intersection angle of 45° in environmental open channel. *International journal of Environmental Science and Technology*, *22*(7), 5543–5554. https://doi.org/10.1007/s13762-024-05953-6

Smith, D. R. (2009). Assessment of in-stream phosphorus dynamics in agricultural drainage ditches. *Science of the Total Environment*, *407*(12), 3883–3889. https://doi.org/10.1016/j.scitotenv.2009.02.038

Song, C. G., Seo, I. W., & Do Kim, Y. (2012). Analysis of secondary current effect in the modeling of shallow flow in open channels. *Advances in Water Resources*, *41*, 29–48. https://doi.org/10.1016/j.advwatres.2012.02.003

Sukhodolov, A. N., & Rhoads, B. L. (2001). Field investigation of three-dimensional flow structure at stream confluences: 2. Turbulence. *Water Resources Research*, *37*(9), 2411–2424. https://doi.org/10.1029/2001WR000317

Sukhodolov, A. N., Shumilova, O. O., Constantinescu, G. S., Lewis, Q. W., & Rhoads, B. L. (2023). Mixing dynamics at river confluences governed by intermodal behaviour. *Nature Geoscience*, *16*(1), 89–93. https://doi.org/10.1038/s41561-022-01091-1

Tsai, W. F., & Ettema, R. (1994). Modified eddy viscosity model in fully developed asymmetric channel flows. *Journal of Engineering Mechanics-ACSE*, *120*(4), 720–732. https://doi.org/10.1061/(ASCE)0733-9399(1994)120:4(720)

Umar, M., Rhoads, B. L., & Greenberg, J. A. (2018). Use of multispectral satellite remote sensing to assess mixing of suspended sediment downstream of large river confluences. *Journal of Hydrology*, *556*, 325–338. https://doi.org/10.1016/j.jhydrol.2017.11.026

Vinuesa, R., Schlatter, P., & Nagib, H. M. (2018). Secondary flow in turbulent ducts with increasing aspect ratio. *Physical Review Fluids*, *3*(5), 24. https://doi.org/10.1103/PhysRevFluids.3.054606

Wang, F. F., Huai, W. X., Liu, M. Y., & Fu, X. C. (2020). Modeling depth-averaged streamwise velocity in straight trapezoidal compound channels with ice cover. *Journal of Hydrology*, *585*, 11. https://doi.org/10.1016/j.jhydrol.2019.124336

Wang, S., Jin, X., Bu, Q., Zhou, X., & Wu, F. (2006). Effects of particle size, organic matter and ionic strength on the phosphate sorption in different trophic lake sediments. *Journal of Hazardous Materials*, *128*(2–3), 95–105. https://doi.org/10.1016/j.jhazmat.2005.07.048

Webber, N. B., & Greated, C. A. (1966). An investigation of flow behaviour at the junction of rectangular channels. *Proceedings - Institution of Civil Engineers*, *34*(3), 321–334. https://doi.org/10.1680/iicep.1966.8925

Xiao, Y., Cheng, H., Zhu, X., & Tang, H. (2015). Experimental study on adsorption of phosphorus on sediment components with different particle sizes. *Environmental Engineering and Management Journal*, *14*(10), 2493–2500. https://doi.org/10.30638/eemj.2015.265

Xiao, Y., Xia, Y., Yuan, S. Y., & Tang, H. W. (2017). Flow structure and phosphorus adsorption in bed sediment at a 90° channel confluence. *Journal of Hydrodynamics, Series B*, *29*(5), 902–905. https://doi.org/10.1016/S1001-6058(16)60804-1

Xiao, Y., Xia, Y., Yuan, S. Y., & Tang, H. W. (2019). Distribution of phosphorus in bed sediment at confluences responding to hydrodynamics. In *Proceedings of the Institution of Civil Engineers-Water Management* (Vol. 172(3), pp. 149–162). https://doi.org/10.1680/jwama.17.00063

Xu, L., Yuan, S., Tang, H., Qiu, J., Xiao, Y., Whittaker, C., & Gualtieri, C. (2022). Mixing dynamics at the large confluence between the Yangtze River and Poyang Lake. *Water Resources Research*, *58*(11), e2022WR032195. https://doi.org/10.1029/2022WR032195

Yakhot, V., & Orszag, S. A. (1986). Renormalization-group analysis of turbulence. I. Basic theory. *Journal of Scientific Computing*, *1*(1), 3–51. https://doi.org/10.1007/BF01061452

Yang, Q., Wang, X., Lu, W., & Wang, X. (2009). Experimental study on characteristics of separation zone in confluence zones in rivers. *Journal of Hydrologic Engineering*, *14*(2), 166–171. https://doi.org/10.1061/(ASCE)1084-0699(2009)14:2(166)

Yang, X., Cheng, H. K., Yu, W. W., & Li, Z. W. (2016). Effects of water flow on the uptake of phosphorus by sediments: An experimental investigation. *Journal of Hydrodynamics, Series B*, *28*(2), 329–332. https://doi.org/10.1016/S1001-6058(16)60636-4

Yu, Q. C., Yuan, S. Y., & Rennie, C. D. (2020). Experiments on the morphodynamics of open channel confluences: Implications for the accumulation of contaminated sediments. *Journal Geophysical Research-Earth Surface*, *125*(9), 25. https://doi.org/10.1029/2019JF005438

Yuan, S., Qiu, J., Tang, H., Xu, L., Xiao, Y., Liu, M., et al. (2023). Fish community traits near a large confluence: Implications for its nodal effects in the river ecosystem. *Journal of Hydrology*, *626*, 130335. https://doi.org/10.1016/j.jhydrol.2023.130335

Yuan, S., Tang, H., Xiao, Y., Xia, Y., Melching, C., & Li, Z. (2019). Phosphorus contamination of the surface sediment at a river confluence. *Journal of Hydrology*, *573*, 568–580. https://doi.org/10.1016/j.jhydrol.2019.02.036

Yuan, S., Xu, L., Tang, H.-W., Xiao, Y., & Gualtieri, C. (2022). The dynamics of river confluences and their effects on the ecology of aquatic environment: A review. *Journal of Hydrodynamics*, *34*(1), 1–14. https://doi.org/10.1007/s42241-022-0001-Z

Yuan, S., Zhu, Y., Tang, H., Xu, L., Li, K., Xiao, Y., & Gualtieri, C. (2022). Planform evolution and hydrodynamics near the multi-channel confluence between the Yarlung Zangbo River and the delta of the Niyang River. *Geomorphology*, *402*, 108157. https://doi.org/10.1016/j.geomorph.2022.108157

Yuan, S. Y., Lin, H., Tang, H. W., Qiu, J. J., Li, Z. P., Xu, D., et al. (2024). An optimized entropy-based model for estimating river confluence hydrodynamics: Accounting for the effects of velocity dip. *Journal of Hydrology*, *628*, 14. https://doi.org/10.1016/j.jhydrol.2023.130408

Yuan, S. Y., Tang, H. W., Xiao, Y., Qiu, X. H., & Xia, Y. (2018). Water flow and sediment transport at open-channel confluences: An experimental study. *Journal of Hydraulic Research*, *56*(3), 333–350. https://doi.org/10.1080/00221686.2017.1354932

Yuan, S. Y., Tang, H. W., Xiao, Y., Qiu, X. H., Zhang, H. M., & Yu, D. D. (2016). Turbulent flow structure at a 90-degree open channel confluence: Accounting for the distortion of the shear layer. *Journal Hydro-Environment Research*, *12*, 130–147. https://doi.org/10.1016/j.jher.2016.05.006

Zhang, T., Feng, M. Q., & Chen, K. L. (2023). The quantitative response of pollutant spatial distribution and mixing dynamics to confluent conditions in an asymmetric open-channel confluence. *Journal of Hydrology*, *620*, 12. https://doi.org/10.1016/j.jhydrol.2023.129479

Zhou, A., Tang, H., & Wang, D. (2005). Phosphorus adsorption on natural sediments: Modeling and effects of pH and sediment composition. *Water Research*, *39*(7), 1245–1254. https://doi.org/10.1016/j.watres.2005.01.026

Zhou, M., Xia, J., Deng, S., Shen, J., & Mao, Y. (2023). Modelling of phosphorus and nonuniform sediment transport in the Middle Yangtze River with the effects of channel erosion, tributary confluence and anthropogenic emission. *Water Research*, *243*, 120304. https://doi.org/10.1016/j.watres.2023.120304